TU Delft

Delft University of Technology

Document Version
Final published version

Licence
CC BY

Citation (APA)
Huang, C., Rueda Torres, J. L., & Kuruveettil, N. N. (2026). Aggregated electrolyzer modeling and coordinated frequency support of multi-GW offshore wind-hydrogen energy systems. *Energy Conversion and Management*, *366*, Article 121862. https://doi.org/10.1016/j.enconman.2026.121862

Important note
To cite this publication, please use the final published version (if applicable).
Please check the document version above.

Copyright
In case the licence states “Dutch Copyright Act (Article 25fa)”, this publication was made available Green Open Access via the TU Delft Institutional Repository pursuant to Dutch Copyright Act (Article 25fa, the Taverne amendment). This provision does not affect copyright ownership.
Unless copyright is transferred by contract or statute, it remains with the copyright holder.

Sharing and reuse
Other than for strictly personal use, it is not permitted to download, forward or distribute the text or part of it, without the consent of the author(s) and/or copyright holder(s), unless the work is under an open content license such as Creative Commons.

Takedown policy
Please contact us and provide details if you believe this document breaches copyrights.
We will remove access to the work immediately and investigate your claim.

*This work is downloaded from Delft University of Technology.*

Energy Conversion and Management 366 (2026) 121862

Contents lists available at ScienceDirect

Energy Conversion and Management

journal homepage: www.elsevier.com/locate/enconman

Research paper

# Aggregated electrolyzer modeling and coordinated frequency support of multi-GW offshore wind-hydrogen energy systems

Chunjun Huang [a], José Luis Rueda Torres [a,*], Nakul Narayanan Kuruveettil [b]

[a] Department of Electrical Sustainable Energy, Delft University of Technology, 2628 CD Delft, The Netherlands
[b] Department of Electrical Engineering, Government Engineering College Thrissur, India

ARTICLE INFO

*Keywords:*
Proton exchange membrane electrolyzer
Offshore wind power plants
High-voltage direct current transmission
Frequency regulation
Real-time digital simulation

ABSTRACT

Multi-gigawatt offshore wind-hydrogen energy systems (OWHESs) extend conventional high-voltage direct-current (HVDC)-connected offshore wind power plants (WPPs) by integrating large-scale electrolyzer plants (ELPs), offering a promising decarbonization path through coupling clean offshore wind and green hydrogen. For OWHES dynamic assessment, ELP models scalable to large plant capacities are needed to preserve key electrical dynamics and capture interactions with HVDC links and WPPs. However, existing studies lack an explicit scale-up modeling method for constructing such models, limiting integrated OWHES dynamic assessment. Moreover, existing frequency controls for HVDC-connected WPPs and ELPs are separately developed, without coordinating their complementary responses, leaving OWHES frequency support under-exploited. To address these gaps, this paper develops a module-based aggregated ELP modeling method and a coordinated fast frequency control strategy for OWHESs. The proposed model derives a capacity-scalable plant-level ELP equivalent through an explicit module-to-plant parameter-aggregation formulation, retaining stack, converter, hydrogen-buffer, and controller dynamics while reducing complexity. The proposed control coordinates HVDC, WPP, and ELP active-power responses, enabling fast frequency support and smooth, automatic post-support recovery. An integrated 2 GW OWHES model is established on a real-time simulator for system-level verification. Results demonstrate that the aggregated ELP model reproduces the detailed model with only 0.02% maximum power-response error, verifying the capacity-scalable ELP modeling. Compared with existing methods, the proposed frequency control achieves higher frequency nadir, lower frequency-change rate, and shorter settling time while avoiding deadband-induced oscillations. These results provide a modeling and control basis for offshore wind–hydrogen hubs to enable renewable power–hydrogen coupling while providing grid support.

## 1. Introduction

The global transition to clean energy requires innovative solutions for renewable integration. Offshore wind is emerging as a key contributor. This is highlighted by ambitious national targets in various countries, such as the Netherlands' goal of 70 GW offshore wind capacity by 2050 [1]. High-voltage direct current (HVDC) transmission is a preferred technology for connecting offshore wind power plants (WPPs) to onshore grids due to its efficiency and reduced losses [2]. However, wind power fluctuations challenge system stability, requiring advanced energy storage and grid-balancing solutions. Hydrogen is a promising option due to its high energy density. This potential has inspired projects like the "offshore energy-hydrogen hubs" in the North Sea [3], leading to offshore wind-hydrogen energy systems (OWHESs). These systems integrate large-scale electrolyzers with offshore WPPs and connect to onshore networks via HVDC transmission. A recent report [3] discusses the key practical challenges for OWHESs, such as system compatibility, infrastructure requirements, and techno-economic viability. Addressing these challenges requires a thorough understanding of the interactions between converter-interfaced assets. This task is challenging due to the tight coupling of those assets including WPPs, electrolyzers, and HVDC systems, which introduces complex dynamics in electromagnetic transient (EMT) time scale. Consequently, developing proper modeling and control strategies is essential to analyze these dynamics and ensure stable operation, realizing the full potential of OWHESs.

Models for HVDC-connected offshore WPPs have been well-established. Various HVDC converter topologies, including two-level, three-level, and modular multilevel converters (MMCs), have been detailed in the literature. These models range from detailed switching circuits to efficient average-value models for system-level studies [2,4,

* Corresponding author.
*E-mail address:* J.L.RuedaTorres@tudelft.nl (J.L. Rueda Torres).

https://doi.org/10.1016/j.enconman.2026.121862
Received 17 October 2025; Received in revised form 5 June 2026; Accepted 30 June 2026
Available online 10 July 2026
0196-8904/© 2026 The Authors. Published by Elsevier Ltd. This is an open access article under the CC BY license (http://creativecommons.org/licenses/by/4.0/).

**Nomenclature**

**Abbreviation**

| | |
|---|---|
| CFE | Communication-free |
| CFFC | Communication-free frequency control |
| ELP | Electrolyzer plant |
| EMT | Electromagnetic transient |
| FFC | Fast frequency control |
| GSC | Grid-side converter |
| HVDC | High-voltage direct current |
| MMC | Modular multilevel converter |
| OWHES | Offshore wind-hydrogen energy system |
| PEM | Proton exchange membrane |
| PLL | Phase-locked loop |
| PWM | Pulse-width modulation |
| RTDS | Real-time digital simulator |
| SAC | Soft activation control |
| WPP | Wind power plant |

5]. Additionally, international working groups like IEC and WECC have developed standardized models for wind turbine technologies, such as the widely-used Type IV turbine [6]. However, OWHESs introduce large-scale electrolyzer plants (ELPs) as additional converter-interfaced dynamic components coupled with HVDC links and WPPs. This makes ELP modeling a key prerequisite for capturing ELP dynamics and their interactions with HVDC links and WPPs in integrated OWHES dynamic assessment. The challenge is nontrivial because commercially available proton exchange membrane (PEM) electrolyzer units typically have capacities of only 1–6 megawatt (MW) [7,8], whereas offshore ELPs may reach hundreds of megawatts or even gigawatt scale. This creates a substantial scale mismatch between MW-scale module models and plant-level OWHES studies, requiring ELP models scalable to large plant capacities while preserving PEM stack response, power-converter dynamics, hydrogen-buffer behavior, and control dynamics relevant to interactions with HVDC links and WPPs.

Existing studies have developed large-scale ELP models through different modeling routes. Some works directly specify plant-level models at the target capacity for frequency-support analysis [9–12]. These models are useful for evaluating system-level frequency response, but their plant-level parameters are generally case-specific and are not derived from an explicit module-to-plant parameter-aggregation method based on available MW-scale PEM module models and parameters. Other works use simulator-specific scaling functions such as transformer scaling in real-time digital simulator (RTDS) to construct large-scale ELP models via scaling-up the power rating of smaller-capacity electrolyzer module models [13,14]. These approaches enable real-time implementation, but the scaling logic is tied to the simulation platform rather than formulated as an explicit module-to-plant aggregation method. Additionally, in the reported integrated OWHES real-time EMT model [14], the ELP stack is represented using a simplified static electrical equivalent and scaled through simulator-specific functions; therefore, key stack and hydrogen-related dynamics are not retained for integrated OWHES dynamic assessment. A recent study further compared aggregated and detailed large-scale ELP models for grid-integration studies [15]. However, the aggregated model is a specific representation for model-adequacy assessment, instead of an explicit scale-up modeling method for constructing capacity-scalable ELP equivalents at different target plant capacities. Process modeling and supervisory-control modeling have also been developed for industrial ELPs [16,17], but they are not intended for EMT-scale electrical equivalencing of ELPs. In parallel, recent review-level studies have classified control-oriented and energy-management-oriented PEM electrolyzer modeling approaches [18,19]. These studies provide useful model taxonomies and comparison references, but they do not provide an explicit module-to-plant aggregation procedure for constructing large-scale ELP equivalent models for EMT-scale system studies. Table 1 summarizes the main plant-scale modeling routes and clarifies the remaining gap.

This comparison identifies the specific modeling issue addressed in this work. Existing large-scale ELP models are commonly built either by directly prescribing parameters for a selected plant capacity or by applying simulator-dependent capacity scaling from a small-capacity electrolyzer model. These routes do not provide an explicit and platform-independent modeling procedure for constructing dynamics-preserving large-scale ELP equivalents from available MW-scale electrolyzer module information. This observation is consistent with the recent review [20], which notes that a systematic aggregation procedure remains unavailable for constructing large-scale stack or plant representations from PEM electrolyzer electrical-circuit models. Therefore, the unresolved modeling issue addressed in this paper lies in how to explicitly parameterize large-scale ELP equivalents from available module-level information while preserving the key EMT-scale dynamics required for integrated OWHES assessment.

Furthermore, extensive studies have addressed operational challenges in offshore HVDC-connected WPPs through advanced control strategies. These efforts target key objectives such as frequency support [21,22], fault ride-through enhancement [23,24], power oscillation damping [25], and DC voltage stability [26]. Among these topics, frequency support control has been widely investigated to improve onshore frequency stability. Existing frequency control frameworks are commonly classified as communication-based or communication-free schemes [22,27]. Communication-based methods [28] send onshore frequency signals to the offshore site via dedicated communication channels, allowing WPPs to respond directly to onshore frequency deviations. However, these methods suffer from communication latency, higher costs, and reliability risks. To address these issues, communication-free schemes [29,30] have been proposed. These schemes use the HVDC DC-link voltage to mirror onshore frequency deviations to the offshore side, enabling frequency support from WPPs. At the wind generator level, commonly adopted strategies include synthetic inertia control [31] and deloading control [32]. The synthetic inertia control releases rotor kinetic energy for temporary frequency support, while deloading control uses pitch-angle or rotor-speed regulation for offering sustained reserves. However, these classical methods often rely on fixed parameters and simple scenarios (e.g. strong grids or monopolar HVDC system). This can lead to suboptimal control performance or a secondary frequency drop during rotor speed recovery [27].

To address these limitations, recent research has focused on improving control performance under complex conditions. For instance, adaptive dual-droop controls [33] have been proposed to dynamically adjust control gains based on operating states. Similarly, distributed cooperative schemes [34] and hierarchical control strategies [35] use consensus algorithms or multi-stage mechanisms to achieve adaptive power allocation. To pursue global optimality of complex multi-terminal HVDC systems, distributed linear quadratic Gaussian (LQG) control [36] and model predictive control [37] have been utilized. These methods optimize power flow among HVDC converters while respecting system constraints. Furthermore, the promising grid-forming (GFM) control has been employed for HVDC and WPPs in the context of weak grids [38–40]. This allows HVDC converters and WPPs to provide instantaneous inertia support without relying on a phase-locked loop (PLL). Additionally, a coordinated control framework is proposed to integrate supplementary frequency response from a battery storage system with those of HVDC and WPP, achieving enhanced frequency support [41].

The above studies provide important foundations for frequency support from HVDC-connected WPPs. However, OWHESs also involve

**Table 1**
Comparison of modeling routes for large-scale PEM electrolyzer plants.

| Modeling route | Plant-scale construction logic | Explicit module-to-plant mapping? | Gap addressed by this work |
|---|---|---|---|
| Direct plant-level parameterization[9–12] | Target-capacity plant model directly specified using plant-level parameters | No | Case-specific plant parameters |
| Simulator-dependent scale-up [13,14] | Large-scale plant model built using simulator-specific scaling functions, e.g., transformer scaling in RTDS | No | Platform-dependent scaling; simplified ELP dynamics in available OWHES verification |
| Specific aggregated representation [15] | Aggregated plant model built to match the total capacity of detailed modules | Limited | No explicit aggregation parameterization |
| Process and supervisory -control modeling [16,17] | Plant model built from process units or multiple stacks for operation/control studies | No | Not intended for EMT-scale electrical equivalencing |
| **Proposed method** | **Large-scale ELP model derived from commercial-scale module models through explicit module-to-plant parameter aggregation with key dynamics preserved** | **Yes** | **Addresses above gaps through explicit module-to-plant scale-up for large-scale ELP modeling** |

**Table 2**
Comparison of representative existing studies and this work related to OWHES frequency support.

| Ref. | Explicit modeling of large-scale ELP | Coordinated control scope | Frequency control methodology | System recovery mechanism | Real-time simulation |
|---|---|---|---|---|---|
| [31] | ✗ | WPP Only | Synthetic inertia control | ✗ | ✗ (Not mentioned) |
| [32] | ✗ | WPP Only | Deloading control | ✗ | ✗ (Not mentioned) |
| [28] | ✗ | HVDC + WPP | CBE[a] inertia + droop control | ✗ | ✗ |
| [29,30] | ✗ | HVDC + WPP | CFE[a] droop control | ✗ | ✗ (SIMULINK) |
| [33,34] | ✗ | HVDC + WPP | Distributed CFE adaptive droop control | ✗ (Wind turbine only) | ✓ (Partial Opal-RT)[d] |
| [35] | ✗ | HVDC + WPP | CFE hierarchical frequency control | ✗ | ✗ (PSCAD) |
| [36] | ✗ | HVDC + WPP | CFE decentralized LQG[b] control | ✗ | ✗ (SIMULINK) |
| [37] | ✗ | HVDC + WPP | CFE hierarchical energy control | ✗ (Wind turbine only) | ✗ (PSCAD) |
| [38] | ✗ | HVDC + WPP | Dual GFM control on HVDC | ✗ | ✗ (PSCAD + small-scale prototype) |
| [40] | ✗ | HVDC + WPP | GFM-based optimal energy utilization control | ✗ (HVDC DC voltage only) | ✗ (PSCAD) |
| [39] | ✗ | WPP | Dual-port GFM control | ✗ (Wind turbine only) | ✗ (Not mentioned) |
| [41] | ✗ | HVDC + WPP + Battery | CFE coordinated control | ✗ (Wind turbine only) | ✗ (PSCAD) |
| [9,10] | ✗ | ELP Only | Inertia + droop control | ✗ | ✗ (SIMULINK) |
| [42] | ✗ | ELP Only | DC-link voltage droop control | ✗ | ✗ (SIMULINK + small-scale prototype) |
| [14] | ✗ | ELP Only | ✗[c] | ✗ | ✓(RTDS)[e] |
| [43] | ✗ | HVDC + WPP + ELP | ✗[c] | ✗ | ✗ (SIMULINK + small-scale prototype) |
| **Our Work** | **✓ (Physics-based, white-box)[f]** | **HVDC + WPP + ELP** | **Coordinated hierarchical control with soft activation** | **✓ System self-recovery** | **✓** |

[a] CBE and CFE denote communication-based and communication-free schemes, respectively.
[b] LQG denotes linear quadratic Gaussian control.
[c] A cross symbol indicates that dynamic frequency control is not considered in the corresponding studies.
[d] The study performs partial real-time simulations using OPAL-RT to validate converter control, but does not present a real-time modeling or dynamic performance assessment of the OWHES.
[e] Although real-time simulations are conducted using RTDS for an offshore wind–electrolyzer hub, the study adopts simplified ELP representations with static electrical stack equivalents and does not address coordinated HVDC–WPP–ELP frequency-support control.
[f] The proposed approach is a physics-based white-box method with explicit mathematical formulations, enabling applicability across different simulation platforms.

large-scale ELPs as controllable electrical loads for hydrogen production, whose frequency-support characteristics differ substantially from those of HVDC-connected WPPs. To clarify the remaining frequency-control issue, Table 2 compares representative existing studies with this work across multiple dimensions. Based on this comparison, existing studies relevant to OWHES frequency-support analysis can be broadly interpreted from three aspects. First, HVDC-connected WPP studies have demonstrated effective communication-free or coordinated frequency support through HVDC–WPP interactions. However, these methods mainly exploit wind-side flexibility and do not explicitly coordinate large-scale ELPs as controllable dynamic assets. Second, ELP frequency-control studies have shown that electrolyzers can contribute to frequency support through local converter control, including proportional–derivative control [9], virtual synchronous machine control [10], and droop control [42]. Nevertheless, these studies typically only focus on ELP-side frequency response and do not address their dynamic coordination with HVDC links and WPPs at the OWHES level. Third, recent offshore energy-hub studies have explored reserve allocation from wind farms and electrolyzers [43], but their focus is mainly on economic reserve optimization instead of seconds-level dynamic frequency control.

These separate developments in frequency-control methods make the direct aggregation of existing HVDC–WPP and ELP frequency-control methods an intuitive solution for enabling OWHES frequency support. However, such direct aggregation does not constitute an OWHES-level coordination framework. Because WPPs and ELPs have different dynamic capabilities, directly superposing their local control responses may impose fast-varying support components on ramp-limited ELPs or leave the WPP power reduction during rotor-speed recovery insufficiently compensated. This can weaken the effective frequency-support capability and cause unfavorable interactions during support withdrawal and recovery. Therefore, the unresolved control issue addressed in this paper lies in coordinating frequency-support activation, fast–slow power allocation between WPPs and ELPs, and smooth post-support recovery under heterogeneous response dynamics.

Beyond modeling and control design, integrated EMT verification is also required to demonstrate the proposed methods and assess OWHES dynamic behavior under multi-asset coupling. As summarized in Table 2, the reviewed studies have mainly verified individual assets or partial subsystems, such as WPP-only, HVDC–WPP, or ELP-side controls, and are mostly implemented using offline simulation tools such as SIMULINK or PSCAD. Prior work has made initial progress toward integrated OWHES real-time EMT modeling using RTDS [14]; however, the reported integrated model still adopts simplified ELP representations with static electrical stack equivalents, omitting key stack and hydrogen-related dynamics. Therefore, the available integrated OWHES verification model does not sufficiently support the assessment and demonstration of interactions among large-scale ELPs, HVDC links, and WPPs under diverse OWHES operating conditions.

Based on the above literature review and the comparative analyses summarized in Tables 1 and 2, the research gaps addressed in this work can be summarized as follows. *(1)* For large-scale ELP modeling, the gap lies in the absence of an explicit and platform-independent parameterized modeling method for constructing dynamics-preserving large-scale ELP equivalents at different target capacities from available MW-scale module information, without relying on case-specific plant parameters or simulator-dependent scaling. *(2)* For OWHES frequency-support control, an OWHES-level coordinated frequency control method is still needed to organize frequency-support activation, dynamic power allocation, and smooth post-support recovery under the heterogeneous response dynamics of HVDC links, WPPs, and ELPs. *(3)* For integrated EMT verification of OWHES dynamic assessment, the gap lies in the lack of an integrated multi-GW OWHES EMT verification model that incorporates dynamics-preserving ELP representations and supports system-level dynamic assessment of electricity–hydrogen coupling, multi-asset interactions, and coordinated frequency-support performance.

To address these research gaps, this paper develops a module-based aggregated ELP modeling method to enable OWHES system-level dynamic performance assessment, proposes a coordinated fast frequency control strategy to improve the grid-support capability of multi-GW OWHESs, and constructs an integrated 2 GW OWHES real-time EMT verification model implemented on RTDS for system-level dynamic assessment. The main contributions are summarized as follows:

- Developing a module-based aggregated modeling method for large-scale PEM-based ELPs. Instead of directly prescribing a model for a given plant capacity, the proposed method derives the equivalent plant rating, electrical RLC parameters, hydrogen-buffer variables, and controller-related parameters from an available MW-scale electrolyzer module model through explicit aggregation relationships. This explicit module-based derivation enables ELP equivalents at different large-scale target capacities to be generated without relying on case-specific plant parameterization or simulator-dependent black-box scaling. Meanwhile, the aggregated representation reduces model complexity by avoiding the explicit representation of hundreds of individual modules, while preserving the dominant dynamics required to capture the plant-level power response.
- Proposing a coordinated fast frequency control framework for OWHES frequency support. The framework integrates: (1) an enhanced communication-free HVDC control with self-recovery to restore the nominal operating point; (2) a hierarchical structure that coordinates WPP and ELP power responses by decomposing the OWHES power-regulation command into fast-varying components for WPPs and slower components for ramp-limited ELPs; and (3) a soft activation mechanism that avoids deadband-induced frequency oscillations during the system recovery phase. Together, these mechanisms coordinate support activation, dynamic power allocation, and post-support recovery, going beyond the direct aggregation of existing local frequency-control methods.
- Constructing an integrated 2 GW OWHES real-time EMT verification model implemented on RTDS for system-level dynamic assessment. The model integrates the proposed dynamics-preserving aggregated ELP representation, MMC-HVDC and WPP models, and the proposed coordinated FFC strategy within a unified system-level setting. This integrated setting enables real-time verification of ELP aggregation accuracy, electricity–hydrogen coupling dynamics, multi-asset OWHES interactions, and coordinated frequency-support performance under diverse operating conditions, thereby addressing the limitations of existing verification models that rely on simplified ELP representations or cover only partial subsystems.

The remainder of this paper is organized as follows: Section 2 describes the OWHES configuration and modeling demands. Section 3 details the proposed module-based aggregated modeling method for large-scale ELPs. Section 4 then presents the primary controller for a single electrolyzer module to enable its fast power regulation. Building upon this foundation, Section 5 develops the proposed coordinated fast frequency control method for the OWHES. In Section 6, the effectiveness of the proposed modeling and control methods is demonstrated through extensive case studies on RTDS. Finally, Section 7 concludes the paper with a summary of key findings and directions for future work.

## 2. OWHES configuration and modeling demand

Aligned with the blueprint of offshore energy-hydrogen hubs in North Sea [3], this paper develops a 2 GW OWHES as shown in Fig.

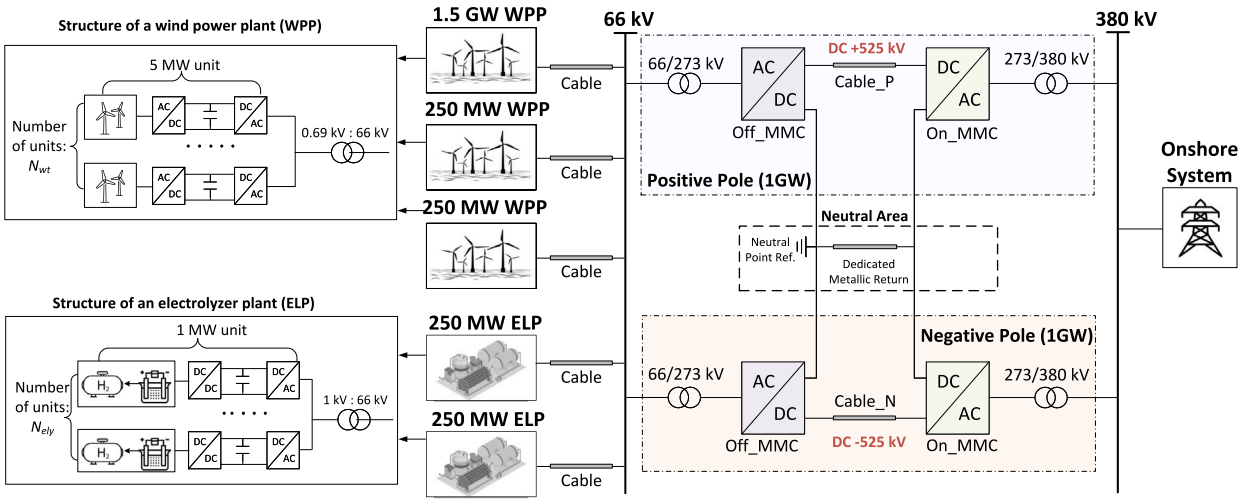



**Fig. 1.** Single-line diagram of the proposed OWHES, based on the 2 GW offshore industrial standardization [44].

1. The offshore wind capacity totals 2 GW, comprising one 1.5 GW WPP and two 250 MW WPPs. Each WPP consists of multiple 5 MW Type IV wind generators. Two 250 MW ELPs consisting of 1 MW PEM electrolyzer units are installed on the offshore side. All WPPs and ELPs are connected via individual cables to a common 66 kV offshore bus. Additionally, a bipolar MMC-based HVDC transmission system links the OWHES to a 380 kV bus connected to the onshore network, enabling electrical energy exchange between offshore and onshore. The adopted bipolar HVDC topology follows the 2 GW offshore industrial standardization in the Netherlands [44,45], employing a dedicated metallic return conductor. The system neutral point is grounded at the offshore station through a grounding switch in series with a neutral grounding resistor to establish a stable potential reference [45]. The rated total transfer capacity of the bipolar HVDC is 2 GW, where the positive pole and negative pole are respectively 1 GW in capacity. The two poles are operated in a symmetric mode by adopting the same structure and control strategies. The onshore converter station (i.e. *On_MMC*) adopts DC voltage and reactive power control, to maintain the power balance of the HVDC system. The offshore converter station (i.e. *Off_MMC*) implements the AC voltage and frequency control to provide voltage and frequency for the offshore system.

Previous studies have developed mature models and control strategies for WPPs and MMC-HVDC systems [2,4–6,22]. However, when large-scale electrolyzers are integrated into OWHESs, existing integrated OWHES dynamic-assessment studies remain limited by simplified ELP representations and platform-dependent scaling. In particular, the available GW-level OWHES real-time EMT study [14] represents the ELP using a simplified static electrical equivalent, without retaining key stack and hydrogen-related dynamics. As a result, a portable and scalable ELP modeling framework remains needed to support detailed EMT-scale OWHES dynamic assessment. To address this, this paper proposes a module-based aggregated model for large-scale ELPs. This model captures EMT-scale dynamics while enabling scalable and platform-independent implementation. The developed ELP model provides a foundation for integrated OWHES modeling and dynamic performance assessment.

## 3. Proposed module-based aggregated modeling for ELPs

### 3.1. Overall modeling framework

The proposed modeling approach adopts a module-based framework widely used in the aggregated modeling of large-scale renewable power plants such as WPPs [46–49]. While the general aggregated modeling philosophy is established and not claimed as new, applying it to PEM-based ELPs requires dedicated methodological adaptations due to the distinct underlying physics. Specifically, WPP aggregation primarily addresses electromechanical dynamics, aerodynamic interactions, and associated power converter circuits, whereas ELPs are governed by strongly coupled electrochemical dynamics (e.g., polarization characteristics and double-layer capacitance effects), power converter dynamics, physical constraints (e.g., power ramping limits) and hydrogen-related dynamics (e.g., hydrogen tank pressure dynamics). As a result, aggregation rules developed for WPPs cannot be directly transferred to ELPs. To address this gap, this paper develops a module-based aggregated modeling method with physics-based mathematical formulations dedicated to large-scale ELPs. The method constructs a plant-level equivalent model from commercial MW-scale PEM modules through explicit module-to-plant parameter aggregation, where the module-level PEM stack, power converter, hydrogen-flow and storage, and controller-related characteristics are mapped into the plant-level representation. Based on this method, the proposed ELP model can effectively represent hundreds of MW electrolysis systems aligned with the planned offshore electrolysis demand in the North Sea [3].

The proposed module-based ELP's topology is shown in Fig. 2. The ELP consists of multiple in-parallel modules that are connected with external AC power grids through a common transformer. The detailed structure of each single module is shown in Fig. 2(b). Each module comprises a hydrogen tank, a PEM electrolyzer stack, and a two-stage power converter (including a grid-side converter and a DC-DC buck converter). In this work, the module is designed as a 1 MW unit, which is a common capacity for commercial PEM electrolyzers. From a modeling perspective, a plant with a capacity of several hundred megawatts can be represented by aggregating multiple modules through a parameter aggregation approach. Here, aggregation refers to mathematical parameter mapping for modeling purposes, rather than physical integration. The latter would involve complex balance-of-plant constraints and is beyond the scope of this work.

The proposed module-based aggregated modeling method for the ELP includes:

- *Dynamic modeling of single electrolyzer module:* captures the dynamic characteristics of individual modules, making it particularly suitable for power system stability studies. This includes implementing EMT modeling for the dynamics of power converters, hydrogen tanks, and multiple electrolyzer stacks operating in parallel.
- *Aggregation of modules:* ensures the scalability of the model, allowing it to represent ELP systems ranging from hundreds of MW to GW-scale capacities.

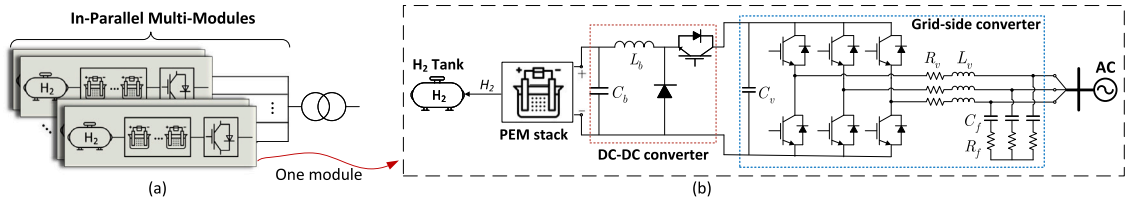



**Fig. 2.** Schematic of the module-based electrolyzer plant: (a) in-parallel multiple modules within the plant; (b) detailed topology of one module.

By combining these two aspects, the proposed modeling method supports both in-depth analysis of single-module behavior and efficient scale-up for large-scale system studies.

### 3.2. Modeling scope and assumptions

Before detailing the electrolyzer dynamic model, the modeling scope and key assumptions are clarified to ensure consistency with the targeted EMT time scale. This study focuses on the EMT behavior and fast frequency control of the OWHES within a milliseconds-to-seconds time scale. Accordingly, the following modeling assumptions are adopted:

(1) *Balance of Plant (BoP):* Slow-varying BoP subsystems, such as thermal management systems, coolant circulation, auxiliary pumps, and compressors, are assumed to remain quasi-constant during short-term frequency regulation events. This assumption is commonly adopted in EMT-based studies of electrolyzers providing fast frequency support [9,10]. This is because these dynamics evolve much more slowly than electrical and frequency responses.

(2) *Model parameterization and scaling assumptions:* The electrolyzer stack parameters are derived from experimental cell data reported in [50]. Based on the validated cell, a typical bipolar stack design is assumed, in which multiple identical cells are connected in series. Besides, inter-cell differences are neglected. The stack model parameters are thus obtained by scaling the validated single-cell parameters. Similarly, at the plant level, the aggregation of multiple electrolyzer modules follows a widely adopted aggregation assumption in the aggregated modeling of large-scale WPPs [46,47,49,51]. Specifically, module-to-module deviations are assumed to be negligible, such that the plant can be represented by an equivalent system-level model. This assumption is consistent with standard practices in EMT-scale power system studies, where aggregation is employed to retain dominant system-level dynamics while ensuring computational efficiency.

(3) *Hydrogen storage:* The hydrogen storage system is modeled as a lumped gaseous buffer tank. While detailed downstream compression technologies and their control dynamics are simplified, the tank pressure is explicitly modeled as a dynamic state. The tank pressure limits impose operational constraints on the electrolyzer power and preserve the key coupling between the hydrogen and electrical domains.

These assumptions enable efficient EMT simulation while retaining the dominant electrical dynamics relevant to fast frequency support. However, it is acknowledged that these assumptions limit the model's applicability to short-term electrical dynamics interacting with power systems. The influence of detailed BoP dynamics and module-to-module deviations becomes more significant at longer time scales and is therefore beyond the scope of this EMT-focused work. These simplifications constitute a modeling limitation of the present study and will be addressed in future research.

### 3.3. Dynamic modeling of single electrolyzer module

The PEM electrolyzer stack model is typically represented by establishing the U-I characteristic, i.e., the relationship between the stack voltage $U_{stack}$ and the stack current $I_s$. For power system dynamics studies, the PEM electrolyzer can be modeled by an equivalent electrical circuit [20,50]. In this context, the widely-used Randles-Warburg cell circuit model [50] is adopted in our work. Based on this cell circuit model and the aforementioned assumptions, the PEM stack is modeled by stacking multiple identical cells in series, as shown in Fig. 3. Accordingly, the stack voltage $U_{stack}$ can be expressed as [20]:

$$U_{stack} = N_{cell}U_{cell} = N_{cell}\left(U_{rev} + \eta_{ohm} + \eta_{act} + \eta_{con}\right) \tag{1}$$

where $N_{cell}$ denotes the number of cells within one single stack; The cell voltage $U_{cell}$ is the sum of the reversible potential and three polarization overpotentials; $U_{rev}$ is the reversible potential; $\eta_{ohm}, \eta_{act}, \eta_{con}$ denote the overpotentials related to ohmic, activation, and concentration polarization effects, respectively. These electrochemical phenomena are mapped to specific circuit elements as follows:

- *Reversible potential ($U_{rev}$):* Represented by the ideal DC voltage source corresponding to the thermodynamic equilibrium potential
- *Ohmic polarization ($\eta_{ohm}$):* Represented by the voltage drop across the series resistor $R_m$, which accounts for the proton conductivity resistance of the membrane and interconnects.
- *Activation polarization ($\eta_{act}$):* Modeled by the voltage across the parallel $R_{act}$-$C_{dl}$ branch. Here, $R_{act}$ represents the charge transfer resistance; the double-layer capacitor $C_{dl}$ captures the dynamic delay of the voltage response due to charge accumulation at the electrode-electrolyte interface.
- *Concentration polarization ($\eta_{con}$):* Represented by the voltage across the Warburg impedance network ($Z_{wbg}$ in Fig. 3, comprising two RC branches $R_1$-$C_{d1}$, $R_2$-$C_{d2}$ in series). This captures the slow dynamic effects of mass transport and diffusion limitations.

The parameters for these circuit elements are identified using the current interrupt method as detailed in [50]. Specifically, the Ohmic resistance $R_m$ is determined via the natural voltage response method where the instantaneous voltage drop ($\Delta V$) observed immediately upon current ($I$) interruption is attributed to purely Ohmic losses (i.e., $R_m = \Delta V / I$). The remaining dynamic parameters ($R_{act}, C_{dl}$, and Warburg impedance values) are then estimated using system identification techniques based on nonlinear least-squares fitting.

Based on the circuit model, the state-space model of the stack is expressed as:

$$\dot{\mathbf{x}} = \mathbf{A}\,\mathbf{x} + \mathbf{B}\,\mathbf{u} \tag{2a}$$

$$\mathbf{y} = \mathbf{C}\,\mathbf{x} + \mathbf{D}\,\mathbf{u} + U_{\text{rev}} \tag{2b}$$

$$\mathbf{x} = \begin{bmatrix} v_{\text{dl}} & v_1 & v_2 \end{bmatrix}^{\mathsf{T}}, \quad \mathbf{u} = I_s, \quad \mathbf{y} = U_{\text{stack}} \tag{2c}$$

where $v_{\text{dl}}$, $v_1$, $v_2$ are the voltage at capacitors $C_{dl}$, $C_{d1}$, $C_{d2}$, respectively. The four coefficient matrices are:

$$\mathbf{A} = \begin{bmatrix} \frac{-1}{C_{dl}R_{act}} & \frac{1}{C_{dl}R_{act}} & \frac{1}{C_{dl}R_{act}} \\ \frac{1}{C_{d1}R_{act}} & \frac{-1}{C_{d1}R_{d1}} + \frac{-1}{C_{d1}R_{act}} & \frac{-1}{C_{d1}R_{act}} \\ \frac{1}{C_{d2}R_{act}} & \frac{-1}{C_{d2}R_{act}} & \frac{-1}{C_{d2}R_{d2}} + \frac{-1}{C_{d2}R_{act}} \end{bmatrix} \tag{3a}$$

$$\mathbf{B} = \begin{bmatrix} \frac{1}{C_{\text{dl}}} & 0 & 0 \end{bmatrix}^{\mathsf{T}}, \ \mathbf{C} = \begin{bmatrix} 1 & 0 & 0 \end{bmatrix}, \ \mathbf{D} = R_m \tag{3b}$$

Compared to the static U-I model used in [14], the developed model can exhibit the dynamic voltage response of electrolyzers due to considering the electrochemical polarization effect, especially the double-layer capacitance effect.

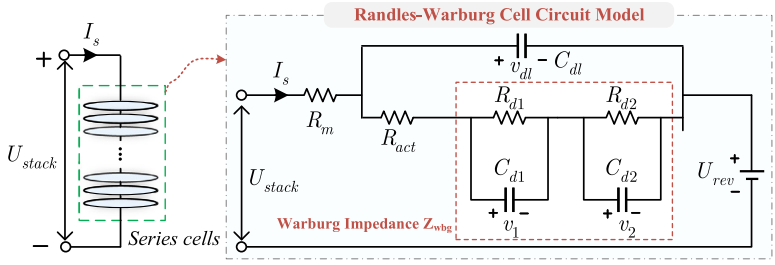



**Fig. 3.** Equivalent electrical circuit model of a PEM stack (based on the parameterized Randles-Warburg cell circuit model in [50]).

The hydrogen production flow from the electrolyzer stack can be calculated according to faraday law, as follows:

$$\dot{n}_{\mathrm{H}_2}^{in} = N_{cell}\frac{\eta_F I_s}{zF} \tag{4}$$

where $z$ is the number of transfer electrons, which is 2; $F$ is the Faraday constant, 96 485 C/mol; $\eta_F$ is the faraday efficiency, which is assumed to be 1.

The produced hydrogen gas from electrolyzer stacks is stored in the hydrogen tank that can hold or supply hydrogen gases for downstream demands. The hydrogen tank model is established to capture the dynamics of internal gas mass $m_{\mathrm{H}_2}$ and pressure $P_{tank}$, which can be expressed by:

$$\frac{1}{M_{\mathrm{H}_2}}\frac{dm_{\mathrm{H}_2}^t}{dt} = \dot{n}_{\mathrm{H}_2}^{in} - \dot{n}_{\mathrm{H}_2}^{out} \tag{5}$$

$$P_{tank} = \frac{m_{\mathrm{H}_2}^t R T_{tank}}{M_{\mathrm{H}_2} V_{tank}} \tag{6}$$

$$P_{t,min} \le P_{tank} \le P_{t,max} \tag{7}$$

where $\dot{n}_{\mathrm{H}_2}^{in}$ and $\dot{n}_{\mathrm{H}_2}^{out}$ are the input and output hydrogen flow of the tank, respectively; $m_{\mathrm{H}_2}^t$ is the hydrogen content inside the tank; $M_{\mathrm{H}_2}$ is the molar mass of hydrogen gas; $V_{tank}$ is the internal volume of the hydrogen tank; $R$ is the ideal gas constant; $T_{tank}$ is the temperature of the tank; $P_{t,min}$ and $P_{t,max}$ are the minimum and maximum pressure of the tank.

The two-stage power converter includes a widely used buck converter and a three-phase pulse-width modulation (PWM) rectifier. The modeling of both converters has been well-developed in previous studies, which can be found in [52].

### 3.4. Aggregation of modules

Directly implementing hundreds of the modules to emulate several-hundred-MW ELPs for EMT analysis, is not practical due to the limitation of computational resources. To address this issue, a general aggregated modeling of multiple modules is developed. As shown in Fig. 4, multiple parallel modules are aggregated into an equivalent plant using the parameter aggregation matrix $\mathbf{M}_{md\to eq}$. The equivalent plant retains the same structure as an individual module. Given the in-parallel connection and neglected differences between modules, the RLC parameters of the aggregated module are obtained by scaling the single-module parameters. Specifically, considering the number of modules as $N_{md}$, the scaling relationships are given by:

$$\mathbf{R}_{eq} = \frac{1}{N_{md}}\mathbf{R}_{md},\ \mathbf{L}_{eq} = \frac{1}{N_{md}}\mathbf{L}_{md},\ \mathbf{C}_{eq} = N_{md}\mathbf{C}_{md} \tag{8}$$

where the subscripts $eq$ and $md$ denote the parameters of the equivalent aggregated model and single module model, respectively; $\mathbf{R}_{md}$, $\mathbf{L}_{md}$ and $\mathbf{C}_{md}$ represent parameter vectors containing the full set of RLC components for a single module (as detailed in Fig. 2). Specifically, these vectors are defined as: $\mathbf{R}_{md} = \begin{bmatrix} R_m & R_{\mathrm{act}} & R_d & R_v & R_f \end{bmatrix}^{\top}$, $\mathbf{L}_{md} = \begin{bmatrix} L_b & L_v \end{bmatrix}^{\top}$, $\mathbf{C}_{md} = \begin{bmatrix} C_{dl} & C_d & C_b & C_v & C_f \end{bmatrix}^{\top}$.

Because the modules are connected in parallel, the aggregated module has the same rated voltage as an individual module, while its rated power scales with the number of modules. Accordingly, it satisfies:

$$S_{eq}^n = N_{md} S_{md}^n \tag{9}$$

where $S_{md}^n$ is the rated power capacity of a single module.

Therefore, the aggregated module model can be established based on the single-module model by adjusting the power rating and impedance parameters (i.e., $R$, $L$, and $C$ values). The matrix $\mathbf{M}_{md\to eq}$ is used to convert the parameters of a single-module model into those of the plant-level equivalent model. Combining (8)–(9), the parameter aggregation matrix $\mathbf{M}_{md\to eq}$ can be formulated as:

$$\begin{bmatrix} S_{eq}^n \\ \mathbf{R}_{eq} \\ \mathbf{L}_{eq} \\ \mathbf{C}_{eq} \end{bmatrix} = \overbrace{\begin{bmatrix} N_{md} & \mathbf{0} & \mathbf{0} & \mathbf{0} \\ \mathbf{0} & \frac{1}{N_{md}}\mathbf{I}_5 & \mathbf{0} & \mathbf{0} \\ \mathbf{0} & \mathbf{0} & \frac{1}{N_{md}}\mathbf{I}_2 & \mathbf{0} \\ \mathbf{0} & \mathbf{0} & \mathbf{0} & N_{md}\mathbf{I}_5 \end{bmatrix}}^{\mathbf{M}_{md\to eq}} \begin{bmatrix} S_{md}^n \\ \mathbf{R}_{md} \\ \mathbf{L}_{md} \\ \mathbf{C}_{md} \end{bmatrix} \tag{10}$$

where $\mathbf{I}_i \in \mathbb{R}^{i\times i}$ is an identity matrix.

Given the same rated voltage as the single module and the relationship (9), the rated impedance and current of the aggregated module can be derived by:

$$Z_{eq}^n = \frac{1}{N_{md}} Z_{md}^n,\quad I_{eq}^n = N_{md} I_{md}^n \tag{11}$$

where $Z_{md}^n$ and $I_{md}^n$ are the rated impedance and current of single module, respectively.

Eqs. (8) and (11) indicate that the plant-level equivalent model's voltage/current variables and RLC parameters retain the same per-unit values as the single module. Consequently, if controllers are designed using a per-unit framework, the well-tuned parameters from a single module can be directly applied to the plant-level equivalent model. This feature avoids additional controller re-tuning after aggregation and simplifies the construction of large-scale ELP models. Table 3 offers an example of this process. It lists the parameters of a 1 MW module and the equivalent 10 MW plant obtained using the aggregation method formulated in (10), where $N_{md} = 10$. As shown, the aggregation is achieved through a systematic scaling of element parameters according to the aggregation matrix $\mathbf{M}_{md\to eq}$. A key advantage lies in the control parameters: when defined in a per-unit framework, the gains of all control loops (e.g., DC voltage, reactive power, and inner current controllers) can be directly reused without modification. This property avoids the need for controller re-tuning and simplifies the aggregation process.

In addition, in the aggregated module, the total amount of produced hydrogen and supplied hydrogen demand can be estimated based on $\dot{n}_{\mathrm{H}_2}^{in}$ and $\dot{n}_{\mathrm{H}_2}^{out}$ in (7), as follows:

$$\dot{n}_{\mathrm{H}_2}^{in,sum} = N_{md}\dot{n}_{\mathrm{H}_2}^{in} \tag{12}$$

$$\dot{n}_{\mathrm{H}_2}^{out,sum} = N_{md}\dot{n}_{\mathrm{H}_2}^{out} \tag{13}$$

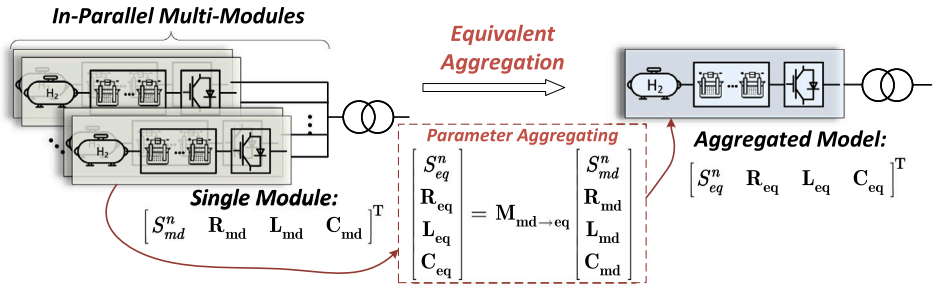



**Fig. 4.** Schematic of module aggregation from multiple in-parallel modules.

**Table 3**
Parameter transformation for a 10 MW ELP using the proposed aggregation method.

| Parameter | Single module[a] | Equivalent plant[b] |
|---|---|---|
| Number of modules ($N_{md}$) | N/A | 10 |
| Rated capacity ($S^n$) | 1 MW | 10 MW |
| Grid-side line-to-line voltage ($V_{ll}$) | 1 kV | 1 kV |
| Grid-side frequency ($f_n$) | 50 Hz | 50 Hz |
| GSC filter capacitor ($C_f$) | 160 μF | 1600 μF |
| GSC filter resistor ($R_f$) | 0.497 Ω | 0.0497 Ω |
| GSC inductor ($L_v$) | 0.63 mH | 0.063 mH |
| GSC resistor ($R_v$) | 0 Ω | 0 Ω |
| DC-link capacitor ($C_v$) | 0.035 F | 0.35 F |
| DC-link voltage ($U_{dc}$) | 2000 V | 2000 V |
| DC-DC converter inductor ($L_b$) | 3.6 mH | 0.36 mH |
| DC-DC converter output capacitor ($C_b$) | 0.01 F | 0.1 F |
| PEM stack rated voltage ($U^n_{stack}$) | 800 V | 800 V |
| PEM stack rated current ($I^n_s$) | 1250 A | 12500 A |
| PEM stack resistor ($R_m$) | 0.0649 Ω | 0.00649 Ω |
| PEM stack resistor ($R_{act}$) | 0.0538 Ω | 0.00538 Ω |
| PEM stack resistor ($R_{d1}$) | 0.0074 Ω | 0.00074 Ω |
| PEM stack resistor ($R_{d2}$) | 0.0681 Ω | 0.00681 Ω |
| PEM stack capacitor ($C_{d1}$) | 0.16889 F | 1.6889 F |
| PEM stack capacitor ($C_{d1}$) | 1.5548 F | 15.548 F |
| PEM stack capacitor ($C_{d2}$) | 20.7 F | 207 F |
| PEM stack reversible voltage ($U_{rev}$) | 558 V | 558 V |
| Number of cells within one stack | 454 | 454 |
| Operating temperature of the validated cell | 80 °C | 80 °C |
| Operating pressure of the validated cell | 1 atm | 1 atm |
| Hydrogen tank temperature ($T_{tank}$) | 350 K | 350 K |
| Hydrogen tank volume ($V_{tank}$) | 100 $m^3$ | 100 $m^3$ |
| *Per-unit controller parameters* | | |
| DC voltage control parameter ($k_{p,dc}, k_{i,dc}$) | 5 p.u., 100 p.u. | 5 p.u., 100 p.u. |
| Reactive power control parameter ($k_{p,Q}, k_{i,Q}$) | 2 p.u., 100 p.u. | 2 p.u., 100 p.u. |
| d-axis current control parameter ($k_{p,id}, k_{i,id}$) | 1.5 p.u., 50 p.u. | 1.5 p.u., 50 p.u. |
| q-axis current control parameter ($k_{p,iq}, k_{i,iq}$) | 1.5 p.u., 50 p.u. | 1.5 p.u., 50 p.u. |
| DC-DC converter control parameter ($k_{p,b}, k_{i,b}$) | 0.1 p.u., 20 p.u. | 0.1 p.u., 20 p.u. |
| GSC PLL parameter ($k_{p,pll}, k_{i,pll}$) | 30 p.u., 200 p.u. | 30 p.u., 200 p.u. |

[a] Parameters for a single 1 MW electrolyzer module.
[b] Calculated parameters for the aggregated equivalent plant ($N_{md} = 10$).

## 4. Primary power controller for electrolyzer module

This section presents the primary power control strategy for the electrolyzer module. The focus is on establishing a reliable DC–DC control interface for large-scale system operation, rather than proposing a new converter-level control structure. This interface allows multi-MW electrolyzer plants to safely provide continuous frequency support within a multi-GW offshore OWHES. To achieve this, a well-established cascaded power–current control structure [10] is adopted. In particular, the control structure is extended by incorporating key physical constraints that limit the electrolyzer power response.

### 4.1. DC-DC converter control

The DC-DC converter regulates the electrolyzer stack's power consumption to achieve rapid power tracking. As shown in Fig. 5, the adopted control scheme consists of a cascaded power–current control architecture. This cascaded structure follows established electrolyzer converter-control practice [10] and is not claimed as a standalone converter-level novelty. In this work, it is adopted as a local actuator interface for the system-level coordinated frequency control developed in Section 5. The power control block processes the initial power reference $P^{ref}_{ely,0}$ through a magnitude and rate limiter, yielding the final power reference $P^{ref}_{ely}$. This reference is converted to an inductor current reference $I^{ref}_L$ according to (14). This current reference is then transferred to the current control block to produce the duty ratio signal $D$ based on (15). Finally, the duty ratio is modulated via PWM to generate switching signals. The adopted power control regulates the electrolyzer power by directly adjusting the input power reference. This allows the electrolyzer module to actively provide frequency support by modifying its power reference in response to grid frequency changes, rather than behaving as a passive load.

$$I^{ref}_L = \frac{P^{ref}_{ely}}{U_{stack}} \tag{14}$$

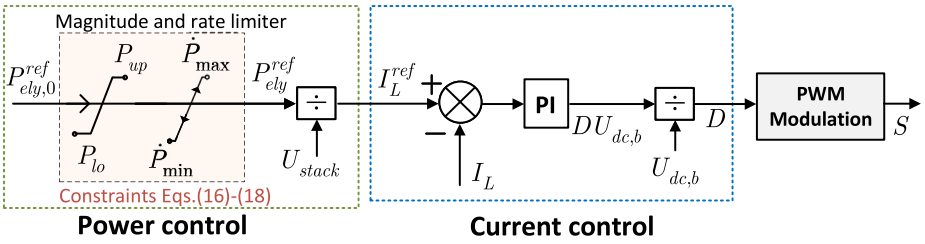



**Fig. 5.** Control structure of the DC-DC converter.

$$D = \frac{k_{p,b}(I_L^{ref} - I_L) + k_{i,b}\int (I_L^{ref} - I_L)dt}{U_{dc,b}} \tag{15}$$

where $k_{p,b}$ and $k_{i,b}$ are the proportional-integral (PI) controller's parameters. $I_L$ is the inductor current; $U_{dc,b}$ is the input DC voltage for the DC-DC converter.

The magnitude and rate limiters, together with the pressure-dependent power bounds, define the executable power reference of the ELP. This local reference translates the upper-level frequency-support command into safe power tracking within ramping, partial-load, and hydrogen-storage constraints. They are introduced to comply with the electrolyzer's physical constraints which reflect trade-offs between efficiency, safety, and lifetime. For instance, rapid power ramping can cause transient overpotentials and local hot spots. This could accelerate degradation of catalysts and membranes [53,54]. Similarly, excessive current density can increase hydrogen permeation through the membrane. This could raise the hydrogen concentration at the anode above safety thresholds [55]. Power bounds $\{P_{min}, P_{max}\}$ and ramping limits $\{\dot{P}_{min}, \dot{P}_{max}\}$ are thus specified by manufacturers to define the allowable operating region. However, due to the additional constraint imposed by (7), the hydrogen tank pressure further influences the operational limits. Specifically, when the tank pressure is near its lower or upper threshold, the safe power bounds must be dynamically adjusted to avoid underproduction or overproduction of hydrogen. Accordingly, the limiter enforces both the fixed ramping limits and the dynamic power bounds as follows:

$$\dot{P}_{min} \le \frac{dP_{ely}^{ref}}{dt} \le \dot{P}_{max},\ P_{lo} \le P_{ely}^{ref} \le P_{up} \tag{16}$$

$$P_{lo} = \begin{cases} \frac{\dot{n}_{H_2}^{out} zF}{\eta_F N_{cell}} U_{stack}, & \text{if } P_{tank} \le P_{t,min} \\ P_{min}, & \text{if } P_{tank} \ge P_{t,min} \end{cases} \tag{17}$$

$$P_{up} = \begin{cases} P_{max}, & \text{if } P_{tank} \le P_{t,max} \\ \frac{\dot{n}_{H_2}^{out} zF}{\eta_F N_{cell}} U_{stack}, & \text{if } P_{tank} \ge P_{t,max} \end{cases} \tag{18}$$

By continuously enforcing both ramping limits and pressure-dependent power bounds, the proposed limiter ensures that electrolyzer modules can remain online and provide the maximum feasible frequency support within safe operating limits. It also avoids abrupt power change (e.g., shut down action due to reaching limits as in [10]) that could affect overall system stability.

### 4.2. Grid-side converter control

The GSC controller uses a widely-used dual-loop control architecture, as shown in Fig. 6. The outer loops in the $d$-axis and $q$-axis stabilize the DC voltage and regulate the reactive power, respectively. These loops generate current references that are passed to the inner control, where decoupled dq-current control is implemented. The inner control produces a voltage reference for the converter, which is then modulated via PWM to generate the switching signals. Detailed implementation of this dual-loop control can be found in [52].

## 5. Proposed coordinated fast frequency control for OWHES

### 5.1. Existing frequency control strategies for OWHES

The conventional communication-free frequency control (CFFC) framework enables HVDC-connected offshore WPPs to respond to onshore frequency deviations without direct communication [22,29,30,33–37]. This is achieved through a two-stage control process using local measurements. First, the onshore converter adjusts its DC voltage reference ($\Delta U_{dc,on}^{ref}$) in proportion to the local onshore frequency deviation ($\Delta f_{on}$). Second, the offshore converter estimates this DC voltage deviation and produces a proportional offshore frequency reference bias ($\Delta f_{off}^{ref}$). These control laws are expressed in (19)–(20). Assuming ideal controller performance, this control process can derive the relationship (21). It confirms the onshore frequency deviation is effectively mirrored on the offshore side.

$$\Delta U_{dc,on}^{ref}(s) = K_1 \Delta f_{on}(s) \tag{19}$$

$$\Delta f_{off}^{ref}(s) = K_2 \left[U_{dc,off}(s) - U_{dc,0} - I_{dc}(s)R_{dc}\right] \tag{20}$$

$$\Delta f_{off} = K_2 K_1 \Delta f_{on}(s) \tag{21}$$

where $I_{dc}$ is the current through the HVDC cable, with the flowing direction to onshore; $R_{dc}$ is the cable resistance; $K_1$ and $K_2$ are positive control gains.

Upon detecting this mirrored frequency deviation, offshore assets like WPPs and ELPs provide frequency support by adjusting their power. Their individual responses are typically governed by dedicated local controllers based on droop and synthetic inertia, as formulated in (22) [56] and (23) [9].

$$\Delta P_{wt,f}^{ref} = K_{p,wt}\left(f_{off} - f_{off,0}\right) + K_{d,wt}\frac{df_{off}}{dt} + K_{i,r}\int \left(\omega_r - \omega_{r,0}\right) dt \tag{22}$$

$$\Delta P_{ely}^{ref} = K_{p,ely}(f_{off} - f_{off,0}) + K_{d,ely}\frac{df_{off}}{dt} \tag{23}$$

where $K_{p,wt}$ and $K_{d,wt}$ are the droop and synthetic inertia parameters, respectively; $K_{i,r}$ is the integral parameter for the rotor speed recovery; $\omega_r$, $\omega_{r,0}$ represent the rotor speed of the wind turbine and its nominal value; $K_{p,ely}$ and $K_{d,ely}$ are the droop and synthetic inertia parameters, respectively.

### 5.2. Proposed coordinated control framework

As summarized in Table 2, the conventional control framework described above primarily enables frequency support through HVDC–WPP coordination, where a system-level self-recovery mechanism is lacking. Moreover, it cannot accommodate the heterogeneous dynamics introduced by large-scale ELPs, particularly the unique power response with electrolyzer physical constraints like power ramping limits. Thus, existing frameworks neither ensure effective coordination between WPPs and ELPs, nor guarantee autonomous recovery of the OWHES to its nominal operating point after a disturbance. To address these fundamental limitations, a coordinated fast frequency control (FFC) framework is proposed, as shown in Fig. 7. In contrast to conventional

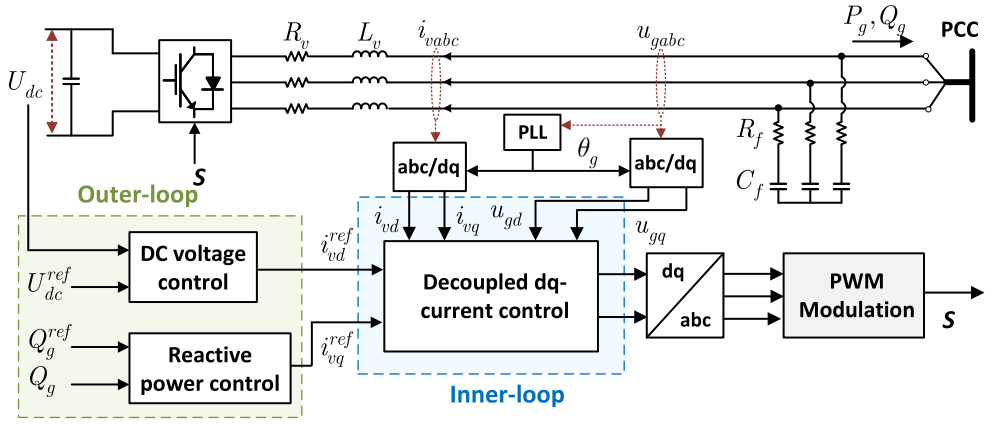



**Fig. 6.** Control structure of the grid-side converter.

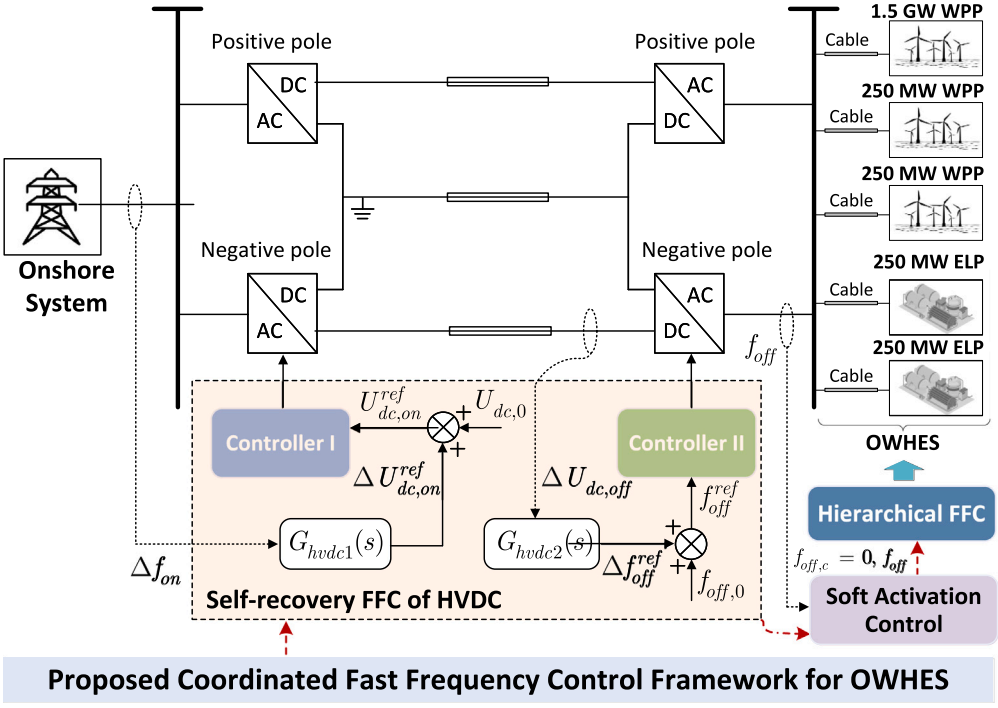



**Fig. 7.** Overall control framework of the proposed fast frequency control.

HVDC–WPP-oriented designs, the proposed framework is developed as a system-level redesign of frequency support coordination under heterogeneous dynamic capabilities. In this framework, soft activation, self-recovery, and coordinated power allocation emerge as interdependent mechanisms driven by the coupled dynamics of the OWHES, rather than added as independent functions. Therefore, the proposed framework goes beyond a direct combination of existing HVDC–WPP and ELP control methods, which has not been addressed by previously reported control frameworks. It should be emphasized that the proposed FFC does not claim novelty in the elementary droop-inertia-based frequency control law, the basic communication-free HVDC control concept, or the generic idea of multi-resource coordination. Instead, its contribution lies in an OWHES-specific coordination synthesis that integrates self-recovery HVDC frequency control, hierarchical WPP–ELP power allocation, and soft activation to avoid recovery-phase oscillations. Appendix B further provides a mechanism-level comparison among existing methods, the simple-combination benchmark, and the proposed coordinated FFC, as shown in Fig. B.1.

The overall control architecture, shown in Fig. 7, consists of three interconnected modules that process the frequency signal in sequence. Together, these modules form an integrated coordination framework that strategically enables heterogeneous frequency response of offshore assets. This is more than a simple aggregation of independent asset controls. The internal coordination mechanism is structured as follows:

- *Module 1–Self-recovery FFC of HVDC*: this module first senses the onshore event and mirrors it to the offshore system via the CFFC framework, generating an offshore frequency deviation ($\Delta f_{off}$). Crucially, by integrating a washout filter, it establishes the foundational condition for the entire OWHES to autonomously return to its nominal operating point. This avoids steady-state offsets introduced by the frequency control action.
- *Module 2–Soft activation control*: this module takes this signal $\Delta f_{off}$ and acts as a smart gate, producing a conditioned frequency signal ($\Delta f_{off,c}$). This conditioning is essential for system-level coordination, as it implements the deadband function to filter out noise and prevents the oscillatory behavior that would otherwise

be triggered by the interaction between the deadband and the recovery dynamics from Module 1.

- *Module 3–Hierarchical fast frequency control*: this module uses the conditioned signal ($\Delta f_{off,c}$) to coordinate the active power responses of offshore assets. The coordination is realized by strategically decomposing the control commands. Fast-varying components of the power command are assigned to the WPPs, while slower components are allocated to the ramp-limited ELPs. This hierarchical allocation is the key to improving the collective frequency response of the offshore assets. This is because it effectively mitigates the impact of the electrolyzer's ramp limits, avoiding mismatches between control commands and the actual power response. In contrast, such mismatches can occur in a simple aggregation of conventional HVDC–WPP control and ELP control, degrading the frequency support capability.

The operating principle of each module is described in detail below:

*(1) Self-recovery FFC of HVDC*

This control module is an improved CFFC for the HVDC system, as depicted in Fig. 7. It not only enables the HVDC system to provide communication-free frequency support but also facilitates the automatic recovery of the OWHES to its pre-disturbance operating state. This self-recovery capability is achieved by integrating a washout filter $\frac{sT_h}{1+sT_h}$ into the onshore converter's control loop. The proposed self-recovery FFC is formulated as:

$$G_{hvdc1}(s) = K_1 \frac{sT_h}{1+sT_h},\ G_{hvdc2}(s) = K_2 \tag{24}$$

$$\Delta f_{off}(s) = K_2 K_1 \frac{sT_h}{1+sT_h} \Delta f_{on}(s) \tag{25}$$

where $T_h$ is the washout filter's time constant;

Accordingly, the steady-state deviations of the DC voltage $\Delta U_{dc,on}$ and offshore frequency $\Delta f_{off}$ can be further derived as (26)–(27). They reveal that both deviations converge to zero in the steady state. It confirms that, after the transient frequency support period, both the HVDC DC voltage and the offshore system frequency autonomously return to their nominal values. As the offshore frequency deviation disappears, the WPPs and ELPs naturally withdraw from frequency support and settle back to their pre-disturbance operating points. Therefore, the entire OWHES achieves self-recovery to its original steady state.

$$\lim_{t\to\infty} \Delta U_{dc,on}(t) = \lim_{s\to 0} sK_1 \frac{sT_h}{1+sT_h} \Delta f_{on}(s) = 0 \tag{26}$$

$$\lim_{t\to\infty} \Delta f_{off}(t) = \lim_{s\to 0} sK_2 K_1 \frac{sT_h}{1+sT_h} \Delta f_{on}(s) = 0 \tag{27}$$

*(2) Soft activation control*

To prevent false activation of frequency control for WPPs and ELPs under normal operation due to minor frequency noise fluctuations, a deadband $[f_{dz,l}, f_{dz,u}]$ is typically applied. For example, the Nordic power system uses 49.99–50.01 Hz for frequency containment reserve [57]. However, combining a conventional deadband with communication-free self-recovery control can lead to oscillations during the system recovery phase. This occurs because frequency support is repeatedly activated and deactivated around the deadband boundary. To address this issue, this paper proposes a soft activation control (SAC) scheme to replace the conventional deadband. The proposed SAC does not introduce new control elements. Instead, it builds on standard control components and provides a dedicated activation logic to eliminate the recovery-induced oscillation behavior. The control logic, shown in Fig. 8, is implemented using fundamental control elements such as a hysteresis buffer, an SR flip-flop, logic gates, and an edge detector. By detecting when the offshore frequency enters and exits the activation region, SAC applies an activation–holding–release logic that withdraws frequency support smoothly during recovery. The proposed SAC preserves the basic function of a deadband: outputting a control signal $f_{off,c}$ that is either the true offshore frequency $f_{off}$ or set as zero, meanwhile effectively eliminating the oscillation observed during recovery.

*(3) Hierarchical fast frequency control*

This control module coordinates frequency support from WPPs and ELPs using a hierarchical structure, as depicted in Fig. 9. The upper layer is responsible for power regulation command calculation and allocation, while the lower layer executes these commands via active power controllers of each electrolyzer module and wind generators. In the upper layer, the total required power regulation ($\Delta P^{ref}_{owhes}$) is first calculated from the frequency signal $f_{off,c}$ according to (28). This total demand is then allocated by decomposing it into slow and fast-varying components. The slow-varying portion $\Delta P^{ref}_{elp,\Sigma}$ obtained via a rate limiter is assigned to the ELPs, while the remaining fast-varying portion $\Delta P^{ref}_{wpp,\Sigma}$ is assigned to the WPPs. This allocation strategy leverages the WPPs' rapid response to compensate for the ramping limitations of the ELPs, ensuring the effective delivery of $\Delta P^{ref}_{owhes}$. Finally, the upper layer dispatches the individual power commands ($\Delta P^{ref}_{elp,i}$) and ($\Delta P^{ref}_{wpp,j}$), by proportionally distributing these group commands according to (29)–(30). Furthermore, the lower-layer controllers of each unit receive these commands and add them to the nominal power setpoints ($P^{n}_{elp,i}$ and $P^{n}_{wpp,i}$) to form the final power references. The local active power controllers then track these references, regulating their active power output to provide the required frequency support.

$$\Delta P^{ref}_{owhes} = K_{p,off}(f_{off,c} - f_{off,0}) + K_{d,off} \frac{df_{off,c}}{dt} \tag{28}$$

$$\Delta P^{ref}_{elp,i} = m_{elp,i} \Delta P^{ref}_{elp,\Sigma},\ i = \{1,2\} \tag{29}$$

$$\Delta P^{ref}_{wpp,j} = m_{wpp,j} \Delta P^{ref}_{wpp,\Sigma},\ j = \{1,2,3\} \tag{30}$$

where $K_{p,off}$ and $K_{d,off}$ are the droop and synthetic inertia parameters for the whole OWHES's frequency control, respectively; $m_{elp,i}$ and $m_{wpp,j}$ are the participation factors for $i$th ELP and $j$th WPP, respectively, satisfying $\sum_i m_{elp,i} = 1$, $\sum_j m_{wpp,j} = 1$. These factors reflect the power regulation capability of each unit and are set proportionally to their rated capacity relative to the total capacity of their respective asset type.

## 6. Case study

The real-time digital simulation of the 2 GW OWHES shown in Fig. 1 is conducted using the commercial real-time digital simulator (i.e. RTDS) with EMT simulation capability. The deployment architecture of this platform is illustrated in Fig. 10. As shown in Fig. 10(a), the system model is constructed in RSCAD. It is then compiled and executed in real time on the RTDS hardware through an Ethernet connection. This setup enables real-time interaction between the system model implemented in RSCAD and the RTDS hardware, allowing the evaluation of the system's dynamic response under real-time conditions. To handle the substantial computational load of the multi-converter system, the model is partitioned using a parallel processing structure, as shown in Fig. 10(b). Chassis 10 uses six of its seven available cores to simulate the onshore system, the HVDC transmission, and the ELPs, while Chassis 11 uses three cores to simulate the WPPs and their collection network. This processor allocation allows the full OWHES model to run in real time with a microsecond-level time step, without processor overruns, enabling stable EMT-level dynamic analysis.

The RTDS platform is used here as a real-time EMT verification environment for the proposed aggregated ELP model and coordinated FFC in an integrated multi-GW OWHES. It enables the proposed modeling and control methods to be examined under real-time execution conditions, including model scalability, system-level dynamic interactions, and frequency-support performance.

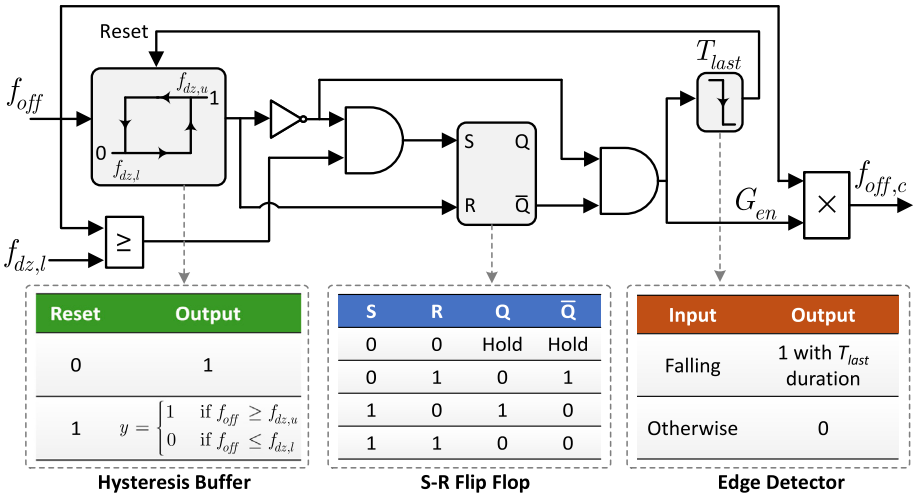



**Fig. 8.** Diagram of the proposed soft activation control.

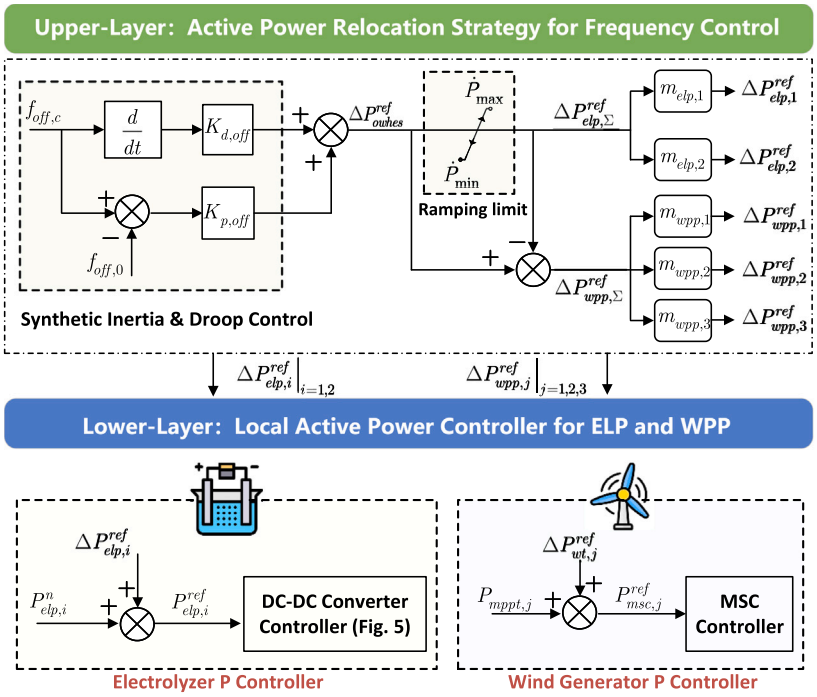



**Fig. 9.** Diagram of the proposed hierarchical fast frequency control for offshore WPPs and ELPs.

### 6.1. Examination for electrolyzer scalability

In this section, the scalability of the proposed aggregated electrolyzer model is examined. The objective is to verify that the model provides accuracy comparable to existing high-fidelity black-box approaches, while retaining the transparency, portability, and computational efficiency of a white-box framework. To this end, a 10 MW ELP is modeled using three approaches: *(1) Detailed Model:* a benchmark by explicitly simulating all ten 1 MW units to capture realistic dynamics; *(2) Aggregated Model:* our proposed aggregated model; and *(3) Existing Scaling Model:* a reference model employing the black-box scaling function in RTDS applied to a single 1 MW unit [14]. The key parameters of the 1 MW electrolyzer unit and the aggregated model are given in Table 3.

As illustrated in Fig. 11, the dynamic responses of the Aggregated Model under power setpoint step changes closely match those of both the Detailed Model and the Existing Scaling Model. The transient deviation in the system-level power response remains within 0.02%. This result indicates that the proposed aggregated model accurately reproduces the plant-level power dynamics. Furthermore, Table 4 compares the computational complexity of the Detailed Model and the proposed model. The Detailed Model requires more than ten times the number of control components and a much larger network matrix than the proposed aggregated model. As a result, it would lead to processor overload and real-time execution failure at small simulation time step (e.g., 30 μs). In contrast, the proposed aggregated model maintains stable real-time performance at the same time step, demonstrating its scalability with superior computational efficiency.

Moreover, the response similarity with the Existing Scaling Model further confirms that the performance of the platform-dependent black-box model can be reproduced using the proposed transparent aggregated model. While the Existing Scaling Model provides similar results, its untransparent structure and platform dependency restrict its general usability.

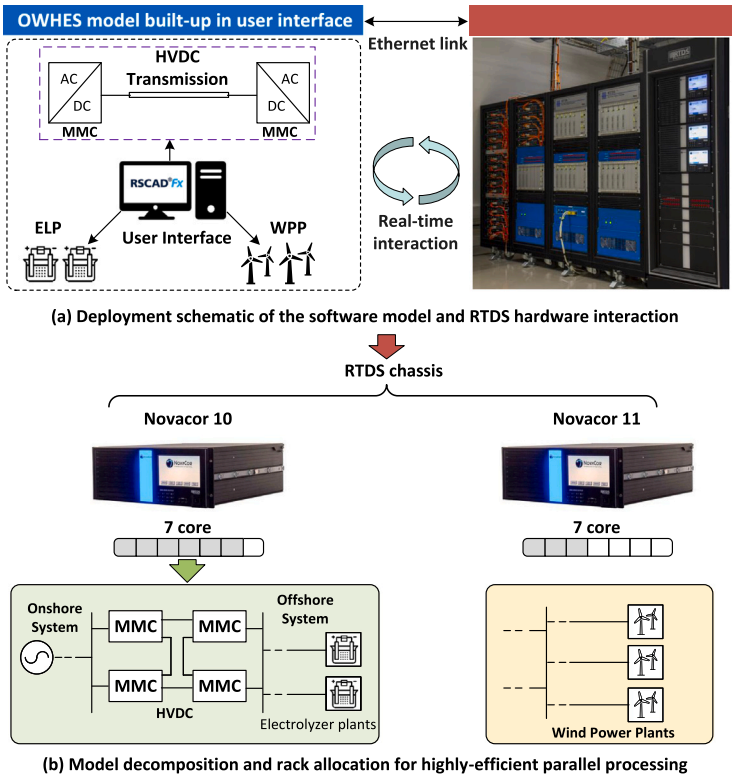



**Fig. 10.** RTDS-based real-time EMT simulation platform and model deployment for the OWHES.

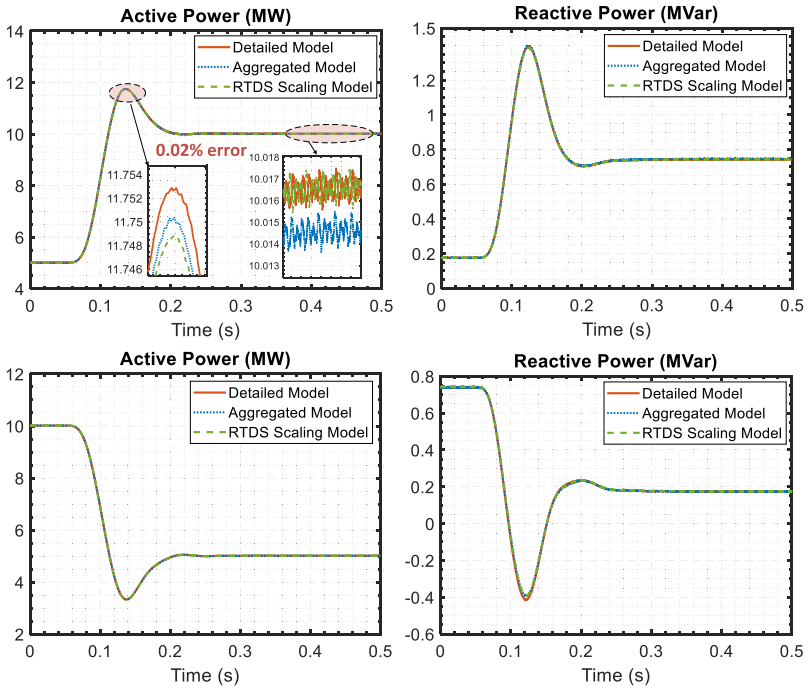



**Fig. 11.** Power response of three electrolyzer models under power setpoint step-up/down changes at $t = 0.06$ s.

Therefore, the contribution of the proposed approach lies not in minor waveform differences, but in its methodological advancement. Overall, the proposed approach systematically addresses these limitations through the following key advantages:

*(1) Scalability and computational efficiency:* Our aggregated model can achieve a comparable accuracy of system-level response compared to the Detailed Model, but greatly reducing computational burden. Thus, this property makes it suitable for multi-GW OWHES studies where simulating a detailed model that integrates hundreds of unit models is impractical.

*(2) Portability:* the model is formulated using explicit mathematical expressions (see Section 3.4), enabling implementation across different simulation environments without reliance on platform-specific functions.

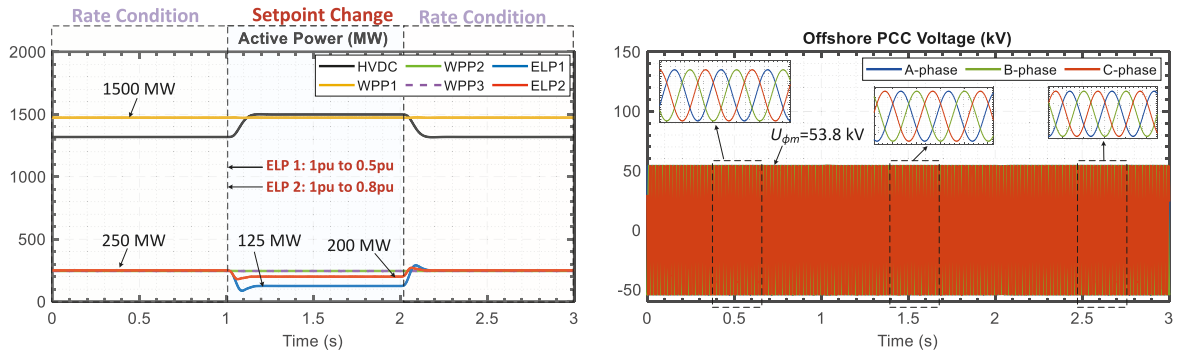



**Fig. 12.** System response under ELP power setpoint changes.

**Table 4**
Comparison of computational complexity between detailed model and the proposed aggregated model.

| Metric | Detailed model | Aggregated model |
|---|---|---|
| Network nodes | 203 | 23 |
| Matrix decomposition size | 133 columns | 16 columns |
| Number of electrolyzer units | 10 | 1 |
| Control components | 4642 | 481 |
| Maximum processor load | Core #2 (overflow) | Core #2 (stable) |
| Real-time performance (time-step is $T_s = 30$ μs) | Overflow | Stable |

*(3) Transparency:* the physics-based white-box structure allows clear interpretation of the model dynamics and facilitates further extension or modification.

In addition, it is important to emphasize that the model's accuracy may deviate from a detailed representation when the assumed homogeneity is violated, such as asymmetrical operation or internal faults.

### 6.2. Performance examination of OWHES under various operation conditions

The dynamic performance of the 2 GW OWHES is further evaluated, with the key system parameters summarized in Table A.1. Each 250 MW ELP is obtained by scaling a 1 MW unit using the proposed aggregation method, following the same parameter derivation procedure as in the 10 MW case shown in Table 3. This assessment examines the correctness of the resulting system-level dynamic response and overall operational behavior of the OWHES, under various operating conditions.

*1. Operating Setpoints Change:*

Fig. 12 shows the OWHES operation under rated conditions and its dynamic response to power setpoint adjustments of two ELPs. Before $t = 1$ s, the system operates at rated conditions. WPP 1 delivers 1.5 GW, while WPP 2 and WPP 3 each deliver 250 MW. The two ELPs each consume 250 MW. Thus, the OWHES remains at its nominal operating point. At $t = 1$ s, the power references of ELP 1 and ELP 2 are reduced to 0.5 pu and 0.8 pu, respectively. The proposed control method for ELPs promptly adjusts their power consumption to 125 MW and 200 MW, accurately tracking the new setpoints. As a result, the reduced ELP demand leads to an increase in the power transferred through the HVDC link to the onshore system. At $t = 2$ s, the ELP power references return to their rated values, and the OWHES swiftly restores its nominal operation. Throughout the entire process, the offshore common bus voltage remains regulated at its rated value (53.8 kV phase voltage, corresponding to a 66 kV line-to-line voltage ). These results demonstrate that the OWHES operates with good stability and is well-controlled to track given setpoints.

*2. Hydrogen Demand Change:*

The effectiveness of the developed ELP's controller is further tested under sudden changes in downstream hydrogen demand, to examine its ability to enforce the hydrogen tank's physical constraints. An extreme scenario is considered where hydrogen demand experiences a step-down while the tank pressure nears its upper limit. The dynamic responses of two ELPs are shown in Fig. 13. At $t = 1.5$ s, the hydrogen output flow decreases from 1150 $Nm^3/h$ to 800 $Nm^3/h$, initiating a gradual rise in tank pressure. During this period, both ELPs continue to operate at their rated setpoint of 250 MW. When the pressure reaches the upper threshold (50 000 Pa) at approximately $t = 5.6$ s, the controller promptly reduces the ELPs' power consumption to about 174 MW. This reduces the hydrogen input flow to 800 $Nm^3/h$, thereby stabilizing the tank pressure at its upper limit and preventing further increase. These results demonstrate that the proposed ELP controller can adaptively regulate electrolyzer power in response to tank pressure variations. Under normal conditions, the ELP power follows the setpoints. When the pressure approaches safety limits, the power setpoint is automatically adjusted to maintain safe pressure levels, thereby ensuring the operational safety of ELPs.

*3. Power Plants Trip:*

Furthermore, the system response and stability under severe disturbances are examined by simulating the simultaneous tripping of the largest 1.5 GW WPP 1 and a 250 MW ELP 1, as shown in Fig. 14. At $t = 0.12$ s, the tripping event causes the generated power of WPP 1 and the consumed power of ELP 1 to drop to zero. The remaining WPPs and ELP 2 continue operating at their rated setpoints. Consequently, the reduced generation from the WPPs leads to a decrease in the HVDC's power transfer to onshore. Following this disturbance, the offshore bus voltage only experiences a short transient lasting several milliseconds and then stabilizes at its rated value. The result demonstrates that, despite the significant disruption, the OWHES can successfully re-establish a new equilibrium by automatically reallocating internal power balance.

Overall, these assessments confirm that the developed real-time simulation model for the 2 GW OWHES can capture EMT-scale system dynamics and exhibits the expected responses under diverse operating conditions, proving its effectiveness. This model thus provides a reliable foundation for the subsequent frequency control performance analysis.

### 6.3. Performance analysis of proposed fast frequency control

This section evaluates the performance of the proposed coordinated FFC during a severe under-frequency event triggered by a 100 MW generator loss in the onshore system at $t = 2$ s. The proposed FFC is compared with existing and simple-combination strategies. Four FFC strategies are considered as follows:

- *No FFC:* no fast frequency control.
- *Conventional FFC:* the existing HVDC–WPP CFFC method [22], where frequency support is provided through HVDC–WPP coordination.

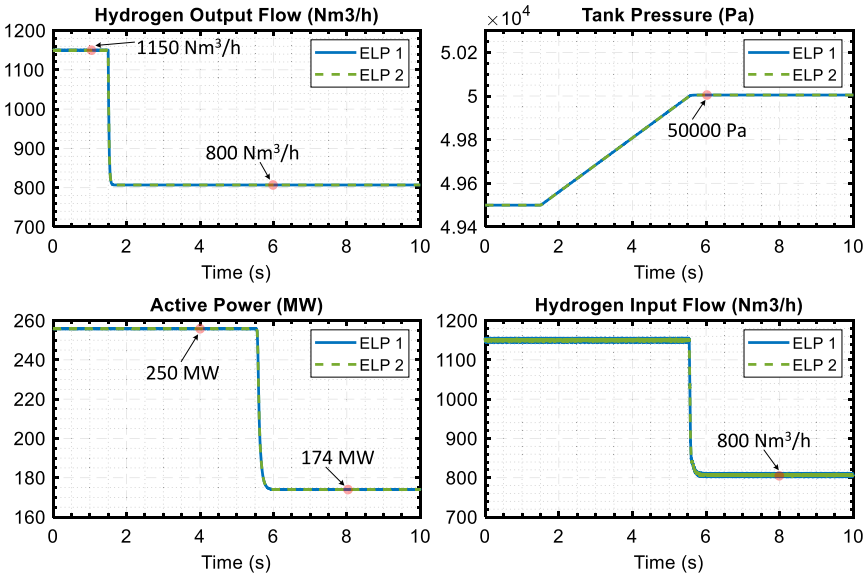



**Fig. 13.** Dynamic response of electrolyzer plants under the hydrogen demand step-down change.

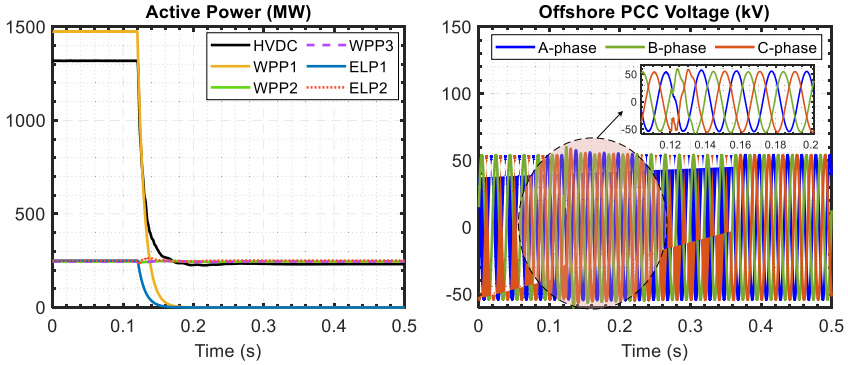



**Fig. 14.** System response under WPP 1 and ELP 1 trip.

- *Aggregated FFC:* a simple-combination benchmark formed by directly adding the existing ELP local FFC [9] to the Conventional FFC, without the proposed hierarchical WPP–ELP coordination.
- *Proposed FFC:* the proposed HVDC–WPP–ELP coordinated FFC method, which integrates self-recovery, soft activation, and hierarchical WPP–ELP power allocation.

The Aggregated FFC benchmark is introduced to directly test whether existing HVDC–WPP and ELP local frequency-control loops can be simply combined for OWHES frequency support. For a fair comparison focused on transient frequency support, all active FFC strategies use identical transient frequency-control parameters and the same washout-based action-withdrawal setting. Therefore, the performance difference mainly reflects the coordination mechanism instead of different droop-inertia gains.

The system frequency responses, depicted in Fig. 15, confirm the effectiveness of the proposed method. Although all FFC strategies improve the frequency response compared to the baseline case (No FFC), the proposed FFC exhibits superior performance. It achieves the highest frequency nadir (i.e., the smallest maximum frequency deviation) and the lowest RoCoF for both onshore and offshore systems, and the shortest settling time for the onshore frequency. Notably, due to the washout filter, the offshore frequency in the proposed method autonomously returns to 50 Hz. This allows the OWHES to recover its pre-disturbance operating state without requiring external reset commands. Finally, as all transient frequency support ceases, the onshore frequency in all cases converges to the same steady state determined by the onshore system's primary frequency response.

The comparison between the Aggregated FFC and the Proposed FFC directly reveals the limitation of simple control aggregation. As shown in Fig. 16, the Aggregated FFC provides weaker support and can even cause a temporary negative power contribution ($\Delta P < 0$) during WPP recovery. This occurs because the ramp-limited ELP cannot compensate quickly enough while the WPP reduces output to restore rotor speed. In contrast, the proposed FFC decomposes the OWHES-level power command by assigning fast-varying components to WPPs and slow, rate-limited components to ELPs. This coordination ensures continuous positive power support throughout the event and enables faster WPP recovery.

Fig. 17 further verifies the effectiveness of the proposed SAC compared with a conventional deadband method. When the frequency recovers near the deadband's lower threshold (49.99 Hz), the conventional deadband repeatedly activates and deactivates frequency support, causing oscillations in both the onshore frequency and WPP active power. In contrast, the proposed SAC coordinates its activation–holding–release logic with the self-recovery frequency signal, enabling smooth withdrawal of frequency support and avoiding recovery-phase oscillations.

## 7. Conclusion

This paper developed a module-based aggregated ELP model, an integrated real-time EMT verification platform, and a coordinated fast

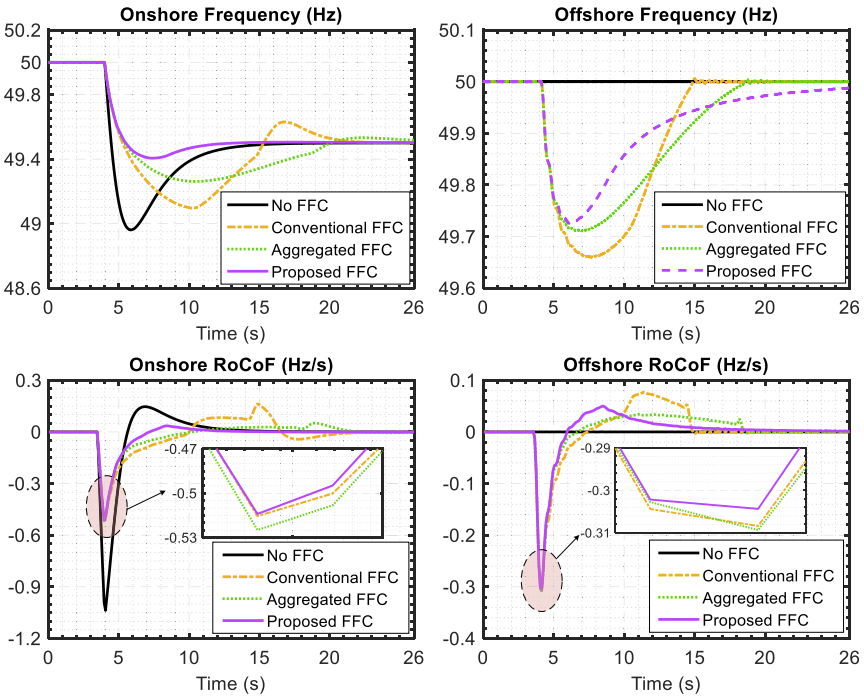



**Fig. 15.** System frequency response under various control strategies.

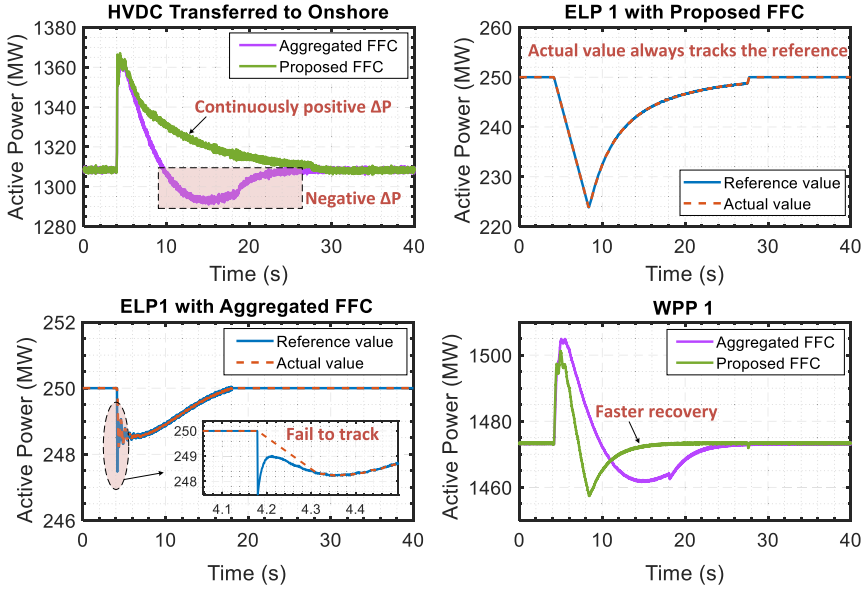



**Fig. 16.** Active power response of the OWHES under the proposed and aggregated FFC strategies.

frequency control framework for multi-GW OWHESs. The aggregated ELP model reproduced the detailed model with only 0.02% maximum power-response error, indicating that the dominant plant-level power dynamics can be preserved after aggregation while avoiding the computational burden of explicitly representing all MW-scale modules. Based on this model, the 2 GW OWHES implemented on RTDS captured the expected dynamic behavior under ELP setpoint changes, hydrogen-demand variations, and plant-tripping events, verifying the platform's capability for real-time assessment of multi-asset dynamic interactions. Furthermore, the proposed coordinated fast frequency control improved the onshore frequency response compared with conventional and simple-combination strategies by increasing the frequency nadir, reducing the rate of change of frequency, and shortening the settling time. It also enabled automatic post-support recovery and avoided deadband-induced oscillations.

These results show that scalable ELP aggregation and coordinated HVDC–WPP–ELP control are both essential for assessing and operating future OWHESs. The modeling results provide a scalable and portable modeling basis for EMT-scale dynamic studies of large-scale ELPs in integrated OWHESs. Furthermore, the control results demonstrate that OWHESs should not be regarded merely as passive renewable-powered hydrogen-production loads. With coordinated control, they can act as flexible offshore energy-hydrogen hubs that integrate renewable power, produce green hydrogen, and support grid stability. Future work will focus on enhancing coordinated frequency control through parameter co-optimization. The scenario will also be extended to longer

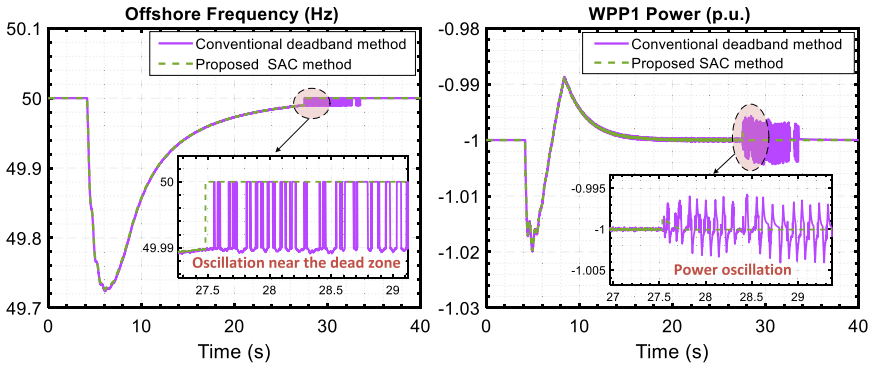



**Fig. 17.** System response under the proposed SAC and a conventional deadband method.

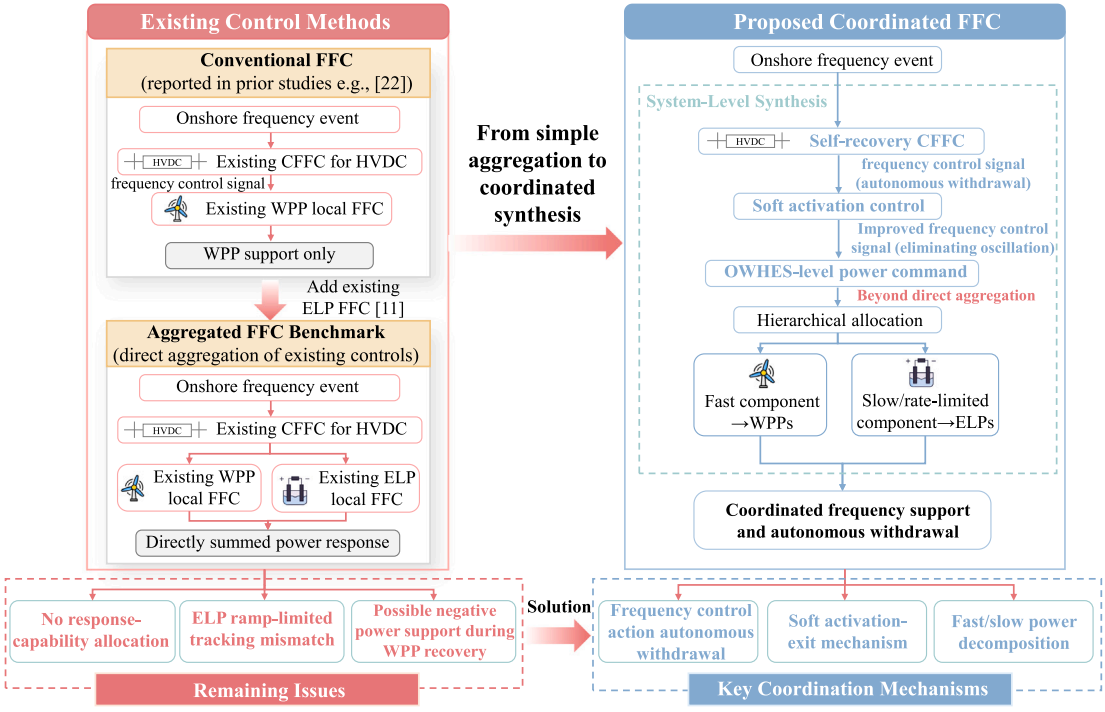



**Fig. B.1.** Mechanism-level comparison of existing FFC methods, the simple-combination benchmark, and the proposed coordinated FFC.

time scales (e.g. secondary and tertiary frequency control), where balance-of-plant dynamics and module-level deviations of ELPs become non-negligible and will be incorporated into the modeling and control design.

## CRediT authorship contribution statement

**Chunjun Huang:** Writing – review & editing, Writing – original draft, Visualization, Validation, Software, Methodology, Investigation, Formal analysis, Data curation, Conceptualization. **José Luis Rueda Torres:** Writing – review & editing, Supervision, Software, Resources, Project administration, Methodology, Investigation, Funding acquisition. **Nakul Narayanan Kuruveettil:** Writing – review & editing, Visualization, Validation, Formal analysis.

## Declaration of competing interest

The authors declare that they have no known competing financial interests or personal relationships that could have appeared to influence the work reported in this paper.

## Acknowledgments

The research work has received funding from TenneT TSO B.V. within the research project on "Adaptive fast active power control for stabilization of multiconverter dynamics in offshore electrical energy-hydrogen hubs - FUTURE SYSTEM". It reflects only the authors' views, and the aforesaid organization is not responsible for any use that may be made of the paper's content.

## Appendix A. System parameters

Table A.1 presents the key parameters of the electrolyzer plants, wind power plants, and the HVDC transmission system.

## Appendix B. Mechanism-level comparison of FFC methods

Fig. B.1 provides a mechanism-level comparison of existing FFC methods, the simple-combination benchmark, and the proposed coordinated FFC. The Conventional FFC represents the existing HVDC–WPP-oriented CFFC method, while the Aggregated FFC benchmark is formed by directly adding an existing ELP local FFC to the Conventional FFC.

**Table A.1**
Key parameters of the 2 GW OWHES, including electrolyzer plants, wind power plants, and the HVDC transmission system.

| Parameter | Value | Unit |
|---|---|---|
| Electrolyzer plants | | |
| Stack rated power | 1 | MW |
| Stack rated voltage | 800 | V |
| Stack rated current | 1250 | A |
| Output voltage of DC–DC converter | 800 | V |
| Input voltage of DC–DC converter | 2000 | V |
| AC-side line-to-line voltage of GSC | 1000 | V |
| DC-link voltage of GSC | 2000 | V |
| AC-side frequency of GSC | 50 | Hz |
| Rated power of electrolyzer plant I | 250 | MW |
| Rated power of electrolyzer plant II | 250 | MW |
| Wind power plants | | |
| Rated turbine capacity | 5 | MW |
| Rated wind speed | 12 | m/s |
| Rated generator voltage | 690 | V |
| DC-link voltage | 1200 | V |
| AC-side voltage | 690 | V |
| AC system frequency | 50 | Hz |
| Rated power of wind power plant I | 1500 | MW |
| Rated power of wind power plant II | 250 | MW |
| Rated power of wind power plant III | 250 | MW |
| HVDC transmission system | | |
| Rated capacity | 2 | GW |
| AC-side voltage of offshore converter station | 273 | kV |
| Offshore PCC voltage | 66 | kV |
| DC-link voltage | 525 | kV |
| Offshore system frequency | 50 | Hz |
| Number of submodules per arm | 200 | – |
| AC-side voltage of onshore converter station | 273 | kV |
| Onshore system voltage | 380 | kV |
| Onshore system frequency | 50 | Hz |

In contrast, the proposed coordinated FFC introduces a system-level coordination mechanism rather than a direct aggregation of asset-level controls.

## Data availability

Data will be made available on request.

## References


[1] Ministerie van Economische Zaken en Klimaat. Kamerbrief windenergie op zee 2030–2050. 2022, Kamerstuk, 16 September 2022. Available at: https://www.rijksoverheid.nl/documenten/kamerstukken/2022/09/16/kamerbrief-windenergie-op-zee-2030-2050.

[2] Korompili A, Wu Q, Zhao H. Review of VSC HVDC connection for offshore wind power integration. Renew Sust Energ Rev 2016;59:1405–14. http://dx.doi.org/10.1016/j.rser.2016.01.064.

[3] North Sea Wind Power Hub. Offshore energy hubs: Blueprints with offshore electrolysis. 2024, Discussion paper. Available at: https://northseawindpowerhub.eu/knowledge/offshore-energy-hubs-blueprints-with-offshore-electrolysis.

[4] Yang B, Liu B, Zhou H, Wang J, Yao W, Wu S, Shu H, Ren Y. A critical survey of technologies of large offshore wind farm integration: Summary, advances, and perspectives. Prot Control Mod Power Syst 2022;7(2):1–3. http://dx.doi.org/10.1186/s41601-022-00239-w.

[5] Flourentzou N, Agelidis VG, Demetriades GD. VSC-based HVDC power transmission systems: An overview. IEEE Trans Power Electron 2009;24(3):592–602. http://dx.doi.org/10.1109/TPEL.2008.2008441.

[6] Honrubia-Escribano A, Gómez-Lázaro E, Fortmann J, Sørensen P, Martin-Martinez S. Generic dynamic wind turbine models for power system stability analysis: A comprehensive review. Renew Sust Energ Rev 2018;81:1939–52. http://dx.doi.org/10.1016/j.rser.2017.06.005.

[7] Cummins Inc. HyLYZER®water electrolyzers. Tech. rep., 2021, Product data sheet. Available at: https://www.cummins.com/sites/default/files/2021-08/cummins-hylyzer-1000-specsheet.pdf.

[8] Siemens Energy. Overview of the PEM Silyzer family. 2020, Presentation, 30 September 2020. Available at: https://4echile.cl/wp-content/uploads/2020/10/20200930-SE-NEB-PEM-Electrolyzer-and-Applications_EW.pdf.

[9] Dozein MG, Jalali A, Mancarella P. Fast frequency response from utility-scale hydrogen electrolyzers. IEEE Trans Sustain Energy 2021;12(3):1707–17. http://dx.doi.org/10.1109/TSTE.2021.3063245.

[10] Dozein MG, De Corato AM, Mancarella P. Virtual inertia response and frequency control ancillary services from hydrogen electrolyzers. IEEE Trans Power Syst 2022;38(3):2447–59. http://dx.doi.org/10.1109/TPWRS.2022.3181853.

[11] Huang C, Zong Y, You S, Træholt C. Analytical modeling and control of grid-scale alkaline electrolyzer plant for frequency support in wind-dominated electricity-hydrogen systems. IEEE Trans Sustain Energy 2022;14(1):217–32. http://dx.doi.org/10.1109/TSTE.2022.3208361.

[12] Phan-Van L, Nguyen Dinh V, Nguyen-Duc T. Universal modelling and analysis of grid-scale electrolysers frequency response in wind-dominated power systems. In: IET conference proceedings CP857. vol. 2023, IET; 2023, p. 8–14. http://dx.doi.org/10.1049/icp.2023.3142.

[13] Tuinema BW, Adabi E, Ayivor PK, García Suárez V, Liu L, Perilla A, Ahmad Z, Rueda Torres JL, van der Meijden MA, Palensky P. Modelling of large-sized electrolysers for real-time simulation and study of the possibility of frequency support by electrolysers. IET Gener Transm Distrib 2020;14(10):1985–92. http://dx.doi.org/10.1049/iet-gtd.2019.1364.

[14] Marchand J, Shetgaonkar A, Rueda Torres JL, Lekic A, Palensky P. Emt real-time simulation model of a 2 GW offshore renewable energy hub integrating electrolysers. Energies 2021;14(24):8547. http://dx.doi.org/10.3390/en14248547.

[15] Heins T, Heynen T, Simon S, Gurumurthy SK, Monti A. Comparison of aggregated and detailed large-scale hydrogen electrolyzer plant models for grid integration studies. In: 23rd wind & solar integration workshop. WIW 2024, vol. 2024, IET; 2024, p. 371–7. http://dx.doi.org/10.1049/icp.2024.3820.

[16] Sakas G, Ibáñez Rioja A, Ruuskanen V, Kosonen A, Ahola J, Bergmann O. Dynamic energy and mass balance model for an industrial alkaline water electrolyzer plant process. Int J Hydrog Energy 2022;47(7):4328–45. http://dx.doi.org/10.1016/j.ijhydene.2021.11.126.

[17] Luxa A, Hanke-Rauschenbach R, Lichtenberg G. Model predictive supervisory control for multi-stack electrolyzers using multilinear modeling. Int J Hydrog Energy 2025;185:151847. http://dx.doi.org/10.1016/j.ijhydene.2025.151847.

[18] Majumdar A, Haas M, Elliot I, Nazari S. Control and control-oriented modeling of PEM water electrolyzers: A review. Int J Hydrog Energy 2023;48(79):30621–41. http://dx.doi.org/10.1016/j.ijhydene.2023.04.204.

[19] Makhsoos A, Kandidayeni M, Ait Ziane M, Boulon L, Pollet BG. Model benchmarking for PEM water electrolyzer for energy management purposes. Energy Convers Manag 2025;323:119203. http://dx.doi.org/10.1016/j.enconman.2024.119203.

[20] Ratib MK, Muttaqi KM, Islam MR, Sutanto D, Agalgaonkar AP. Electrical circuit modeling of proton exchange membrane electrolyzer: The state-of-the-art, current challenges, and recommendations. Int J Hydrog Energy 2024;49:625–45. http://dx.doi.org/10.1016/j.ijhydene.2023.08.319.

[21] Liu H, Chen Z. Contribution of VSC-HVDC to frequency regulation of power systems with offshore wind generation. IEEE Trans Energy Convers 2015;30(3):918–26. http://dx.doi.org/10.1109/TEC.2015.2417130.

[22] Lin C-H, Wu Y-K. Overview of frequency-control technologies for a VSC-HVDC-integrated wind farm. IEEE Access 2021;9:112893–921. http://dx.doi.org/10.1109/ACCESS.2021.3102829.

[23] Silva B, Moreira CL, Leite H, Lopes JP. Control strategies for AC fault ride through in multiterminal HVDC grids. IEEE Trans Power Deliv 2014;29(1):395–405. http://dx.doi.org/10.1109/TPWRD.2013.2281331.

[24] Peñalba MA, Gomis-Bellmunt O, Martins M. Coordinated control for an offshore wind power plant to provide fault ride through capability. IEEE Trans Sustain Energy 2014;5(4):1253–61. http://dx.doi.org/10.1109/TSTE.2014.2344172.

[25] Pipelzadeh Y, Chaudhuri NR, Chaudhuri B, Green TC. Coordinated control of offshore wind farm and onshore HVDC converter for effective power oscillation damping. IEEE Trans Power Syst 2016;32(3):1860–72. http://dx.doi.org/10.1109/TPWRS.2016.2581984.

[26] Jeong B-C, Kwon D-H, Park J-Y, Kim Y-J, Gomis-Bellmunt O. Optimal secondary control to suppress voltage fluctuations in an HVDC-linked wind farm grid. IEEE Trans Power Syst 2021;37(4):2563–77. http://dx.doi.org/10.1109/TPWRS.2021.3123790.

[27] Khan A, Seyedmahmoudian M, Raza A, Stojcevski A. Analytical review on common and state-of-the-art FR strategies for VSC-MTDC integrated offshore wind power plants. Renew Sustain Energy Rev 2021;148:111106. http://dx.doi.org/10.1016/j.rser.2021.111106.

[28] Miao Z, Fan L, Osborn D, Yuvarajan S. Wind farms with HVDC delivery in inertial response and primary frequency control. IEEE Trans Energy Convers 2010;25(4):1171–8. http://dx.doi.org/10.1109/TEC.2010.2060202.

[29] Phulpin Y. Communication-free inertia and frequency control for wind generators connected by an HVDC-link. IEEE Trans Power Syst 2011;27(2):1136–7. http://dx.doi.org/10.1109/TPWRS.2011.2175817.

[30] Silva B, Moreira C, Seca L, Phulpin Y, Lopes JP. Provision of inertial and primary frequency control services using offshore multiterminal HVDC networks. IEEE Trans Sustain Energy 2012;3(4):800–8. http://dx.doi.org/10.1109/TSTE.2012.2199774.

[31] Ochoa D, Martinez S. Fast-frequency response provided by DFIG-wind turbines and its impact on the grid. IEEE Trans Power Syst 2017;32(5):4002–11. http://dx.doi.org/10.1109/TPWRS.2016.2636374.

[32] Margaris ID, Papathanassiou SA, Hatziargyriou ND, Hansen AD, Sorensen P. Frequency control in autonomous power systems with high wind power penetration. IEEE Trans Sustain Energy 2012;3(2):189–99. http://dx.doi.org/10.1109/TSTE.2011.2174660.

[33] Xiong Y, Yao W, Shi Z, Fang J, Ai X, Wen J, Cheng S. Adaptive dual droop control of MTDC integrated offshore wind farms for fast frequency support. IEEE Trans Power Syst 2022;38(3):2525–38. http://dx.doi.org/10.1109/TPWRS.2022.3179504.

[34] Xiong Y, Yao W, Yao Y, Fang J, Ai X, Wen J, Cheng S. Distributed cooperative control of offshore wind farms integrated via MTDC system for fast frequency support. IEEE Trans Ind Electron 2022;70(5):4693–704. http://dx.doi.org/10.1109/TIE.2022.3183355.

[35] Yang X, Li S, Meng Z, Wang Z, Deng Z. Active support capability improvement strategy of offshore wind power through MMC-HVDC based on frequency convey hierarchical control. Electr Power Syst Res 2026;252:112356. http://dx.doi.org/10.1016/j.epsr.2025.112356.

[36] Kim J-S, Kim Y-J, Gomis-Bellmunt O. Optimal frequency regulation of multi-terminal HVDC-linked grids with deloaded offshore wind farms control. IEEE Trans Sustain Energy 2023;15(1):290–303. http://dx.doi.org/10.1109/TSTE.2023.3283525.

[37] Zhang H, Xiang W, Wang Y, Xu Y, Wen J. Hierarchical energy control of MMC-MTDC system integrated with offshore wind farms for optimal frequency support provision. IEEE Trans Power Deliv 2025;40(6):3672–83. http://dx.doi.org/10.1109/TPWRD.2025.3622732.

[38] Zhang H, Xiang W, Wen J. Dual grid-forming control with energy regulation capability of MMC-HVDC system integrating offshore wind farms and weak grids. IEEE Trans Power Syst 2023;39(1):261–72. http://dx.doi.org/10.1109/TPWRS.2023.3244807.

[39] Lyu X, Groß D. Grid forming fast frequency response for PMSG-based wind turbines. IEEE Trans Sustain Energy 2023;15(1):23–38. http://dx.doi.org/10.1109/TSTE.2023.3263858.

[40] Zhang H, Xiang W, He Y, Wen J. Optimal energy utilization of MMC-HVDC system integrating offshore wind farms for onshore weak grid inertia support. IEEE Trans Power Syst 2023;39(1):1304–18. http://dx.doi.org/10.1109/TPWRS.2023.3239166.

[41] Lin C-H, Wu Y-K. Coordinated frequency control strategy for VSC-HVDC-connected wind farm and battery energy storage system. IEEE Trans Ind Appl 2023;59(5):5314–28. http://dx.doi.org/10.1109/TIA.2023.3289939.

[42] Agredano-Torres M, Zhang M, Söder L, Xu Q. Decentralized dynamic power sharing control for frequency regulation using hybrid hydrogen electrolyzer systems. IEEE Trans Sustain Energy 2024;15(3):1847–58. http://dx.doi.org/10.1109/TSTE.2024.3381491.

[43] del Pozo Gonzalez H, Bianchi FD, Cutululis NA, Dominguez-Garcia JL. Providing frequency support to offshore energy hubs using hydrogen and wind reserves. Energy Convers Manag 2025;343:120139. http://dx.doi.org/10.1016/j.enconman.2025.120139.

[44] Alefragkis A, Kabul S. Next generation offshore grid connection systems: TenneT's 2 GW standard. 2022, CIGRE Electra, No. 321. TenneT TSO B.V. Available at: https://electra.cigre.org/321-april-2022/technology-e2e/next-generation-offshore-grid-connection-systems-tennets-2-gw-standard.html.

[45] Love G, Düllmann P, Klein C. Expandable & compatible HVDC grid design. Tech. Rep. 1–118686, Palo Alto, CA: EPRI; 2024, Prepared with RWTH Aachen University for the North Sea Wind Power Hub. Available at: https://northseawindpowerhub.eu/knowledge/expandable-compatible-hvdc-grid-design.

[46] Wu Y-K, Zeng J-J, Lu G-L, Chau S-W, Chiang Y-C. Development of an equivalent wind farm model for frequency regulation. IEEE Trans Ind Appl 2020;56(3):2360–74. http://dx.doi.org/10.1109/TIA.2020.2974418.

[47] Zou J, Peng C, Yan Y, Zheng H, Li Y. A survey of dynamic equivalent modeling for wind farm. Renew Sustain Energy Rev 2014;40:956–63. http://dx.doi.org/10.1016/j.rser.2014.07.157.

[48] Shabanikia N, Nia AA, Tabesh A, Khajehoddin SA. Weighted dynamic aggregation modeling of induction machine-based wind farms. IEEE Trans Sustain Energy 2021;12(3):1604–14. http://dx.doi.org/10.1109/TSTE.2021.3057854.

[49] Brochu J, Larose C, Gagnon R. Validation of single-and multiple-machine equivalents for modeling wind power plants. IEEE Trans Energy Convers 2010;26(2):532–41. http://dx.doi.org/10.1109/TEC.2010.2087337.

[50] Martinson CA, Van Schoor G, Uren KR, Bessarabov D. Characterisation of a PEM electrolyser using the current interrupt method. Int J Hydrog Energy 2014;39(36). http://dx.doi.org/10.1016/j.ijhydene.2014.09.153.

[51] Kunjumuhammed LP, Pal BC, Oates C, Dyke KJ. The adequacy of the present practice in dynamic aggregated modeling of wind farm systems. IEEE Trans Sustain Energy 2016;8(1):23–32. http://dx.doi.org/10.1109/TSTE.2016.2563162.

[52] Erickson RW, Maksimovic D. Fundamentals of power electronics. Springer Science & Business Media; 2001, http://dx.doi.org/10.1007/b100747.

[53] Jung HY, Jun YS, Lee K-Y, Park HS, Cho SK, Jang JH. Effect of ramping rate on the durability of proton exchange membrane water electrolysis during dynamic operation using triangular voltage cycling. J Electrochem Sci Technol 2024;15(2). http://dx.doi.org/10.33961/jecst.2023.00948.

[54] Wallnöfer-Ogris E, Grimmer I, Ranz M, Höglinger M, Kartusch S, Rauh J, Macherhammer M-G, Grabner B, Trattner A. A review on understanding and identifying degradation mechanisms in PEM water electrolysis cells: Insights for stack application, development, and research. Int J Hydrog Energy 2024;65:381–97. http://dx.doi.org/10.1016/j.ijhydene.2024.04.017.

[55] Trinke P, Bensmann B, Hanke-Rauschenbach R. Current density effect on hydrogen permeation in PEM water electrolyzers. Int J Hydrog Energy 2017;42(21):14355–66. http://dx.doi.org/10.1016/j.ijhydene.2017.03.231.

[56] Tang Y, Yang P, Yang Y, Zhao Z, Lai LL. Fuzzy adaptive frequency support control strategy for wind turbines with improved rotor speed recovery. IEEE Trans Sustain Energy 2023;15(2):1351–64. http://dx.doi.org/10.1109/TSTE.2023.3344278.

[57] Nordic Analysis Group. Overview of frequency control in the Nordic power system. Tech. rep., ENTSO-E AISBL; 2024, Report, 7 May 2024. Available at: https://eepublicdownloads.blob.core.windows.net/public-cdn-container/clean-documents/SOC%20documents/Nordic/2024/Overview_of_Frequency_Control_in_the_Nordic_Power_System.pdf.